

# Properties of Ice-Supersaturated Layers Based on Radiosonde Data Analysis

S. L. Baughcum\*, M. Y. Danilin  
*The Boeing Company, Seattle, WA, USA*

L. M. Miloshevich, A. J. Heymsfield  
*National Center for Atmospheric Research, Boulder, CO, USA*

**Keywords:** ice supersaturation, contrail, cirrus, radiosonde

**ABSTRACT:** In order to better understand upper tropospheric humidity and formation of persistent contrails, we analyzed radiosonde sounding data from selected stations of the US National Weather Service for a five year period. We used 55,177 individual corrected Vaisala RS80-H profiles over 15 USA stations from September 2000 to September 2005 for our analysis. These corrections are critical when investigating ice supersaturation in the upper troposphere. Using these corrected measurements for each season and location, we calculated key parameters of ice supersaturated layers (ISSLs): geometric thickness, frequency, and number of ice supersaturated layers per profile along with their probability distributions. The implications of these results are discussed in relation to contrail formation and mitigation.

## 1 INTRODUCTION

For contrails to form, the modified Appleman criterion (Schumann, 1996) which relates propulsion efficiency, fuel properties and ambient conditions must be satisfied. While supersaturation with respect to ice is not required to form a contrail, it is necessary for the contrail to persist for long times. Spichtinger et al. (2003) evaluated radiosonde data of relative humidity over Lindenberg, Germany and showed that the mean ice supersaturated layer (ISSL) thickness was  $560 \pm 610$  meters. Rädel and Shine (2007) performed a similar analysis for radiosonde sites in the United Kingdom and showed an ISSL thickness of 900-1300 m. Mannstein et al. (2005) suggested that small changes in flight altitude could move an aircraft out of the ISSL and reduce contrail impact.

In this paper, we evaluate ISSL properties over the United States with particular emphasis on conditions where contrails will both form and persist.

## 2 APPROACH

Radiosonde data for 13 sites [Blacksburg, Boise, Buffalo, Denver, Flagstaff, Grand Junction, Miami, Norman, Peachtree, Reno, Salt Lake City, Springfield, and Wilmington] in the continental United States plus Lihue (Hawaii) and Fairbanks (Alaska), were obtained from the US National Weather Service for the time period from September 2000 to September 2005. These soundings were made every 12 hours, recorded temperature and relative humidity with respect to water every 6 seconds, and used Vaisala RS80-H sondes. A total of 55,177 soundings were processed with 4,657 profiles rejected mostly because of sensor icing.

A temperature dependent error correction (Wang et al., 2002) and a time-lag correction (Miloshevich et al., 2004) are required for the RS80-H sondes when processing humidity data at the cold temperatures usually encountered in the upper troposphere. The response times of RS92, RS80-H and RS80-A radiosondes are shown in Figure 1a. Figure 1b shows an example highlighting that the time-lag correction can be critical when investigating ice supersaturation in the upper troposphere and that the temperature dependent correction alone is not enough. We use a very simple

---

\* Corresponding author: Steven L. Baughcum, Boeing Company, MC 0R-MT, P. O. Box 3707, Seattle, WA 98124 USA. Email: Steven.L.Baughcum@boeing.com

definition of an ISSL as a layer where the relative humidity with respect to ice (RHi) is greater than 100%. We define a contrailing ISSL (CISSL) as an ISSL where the Appleman criterion is satisfied as well.

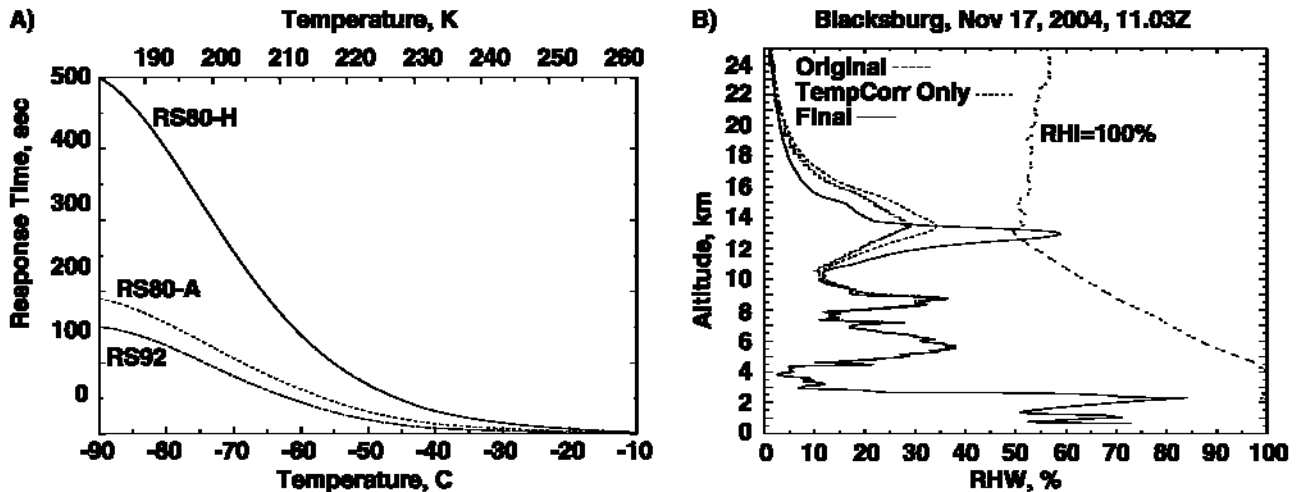


Figure 1. a.) The response time of RS92, RS80-H, and RS80A radiosondes as a function of temperature. b.) The vertical profiles of relative humidity for Blacksburg, VA, on 17 November 2004 at 11Z for the uncorrected data (dashed line labelled as Original), temperature dependence correction only (dotted line labelled as TempCorr only), and with both the temperature dependent and time-lag corrections (solid line labelled as Final). The dashed line on the right corresponds to ice supersaturation [RHi = 100%] for the measured temperature profile.

### 3 RESULTS

Ice supersaturated regions can occur at temperatures which are too warm for contrail formation. This is illustrated in Figure 2 which shows the average probability of ice supersaturation (marked as no Appleman) over Denver (Colorado), in the summer and winter as a function of altitude. Superimposed on the plots is the probability profile when the modified Appleman criterion is applied to identify cases where contrails would form. For these plots, a propulsion efficiency of 30% was assumed. At the higher, colder altitudes, most ISSLs will also lead to contrails but at the lower altitudes (especially in summer) many ISSLs are too warm to form contrails. Similar analyses were done for all the sites but these will be discussed in more depth in a future publication. This figure illustrates the importance of the modified Appleman criterion and the difference between ISSL and contrailing ISSLs (CISSLs).

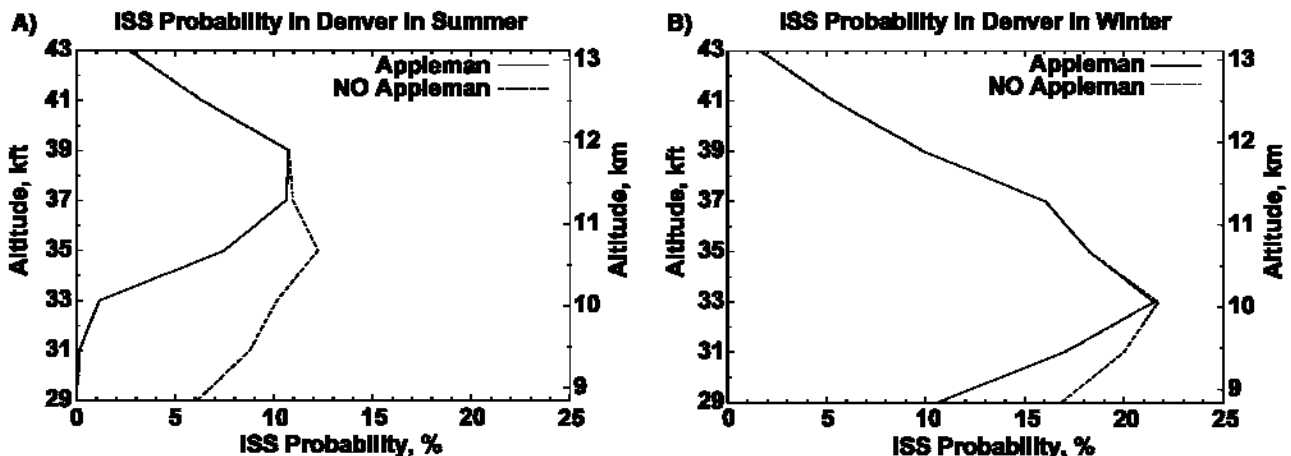


Figure 2. Ice supersaturation probability as a function of altitude over Denver (Colorado) for summer (left panel) and winter (right panel). The solid and dashed lines correspond to the probability with and without the modified Appleman criterion for contrail formation, respectively.

Figure 3a shows the probability distribution of the CISSL thickness over Denver at 35 kft (10.7 km, flight level 350) over the 5 year data period. Figure 3b depicts vertical profiles of the median CISSL thickness over the 15 US locations studied. These results reveal that the median CISSL thickness changes from 0.7-1.2 km at 9 km to 0.3-0.8 km at 13 km, which is consistent in general with the earlier findings of Spichtinger et al. (2003) and Rädel and Shine (2007) for ISSLs over Europe. The studies use different geographical locations, different time periods and different methodologies hampering direct comparison of results.

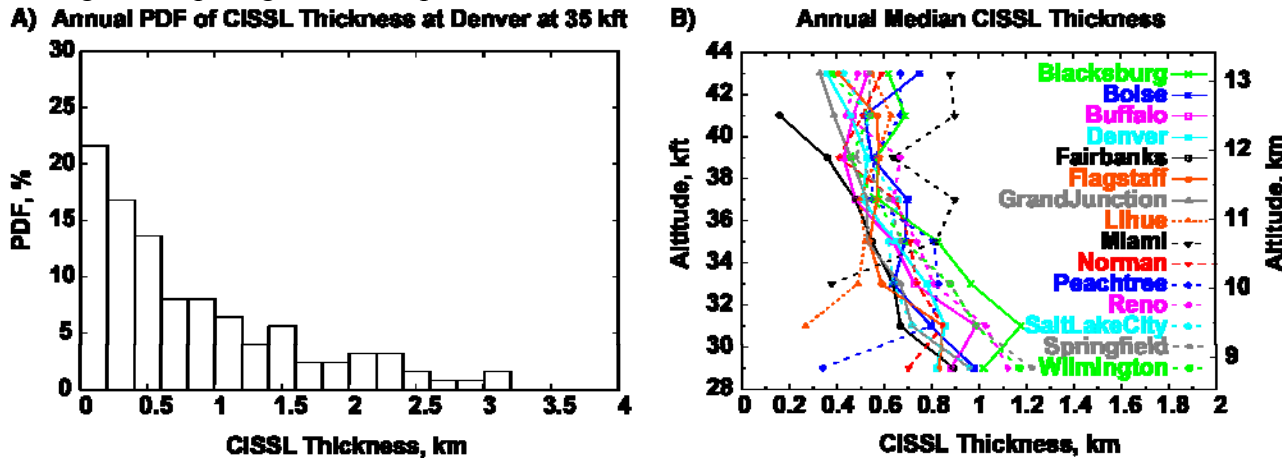


Figure 3. a.) The probability distribution function of the CISSL thickness over Denver (Colorado) at flight level 350 (35 kft or 10.7 km altitude) over the 5 year data period. b.) Annual median thickness of contrailing ISSL as a function of altitude for the 15 sites studied.

We analyzed the number of ice supersaturated layers per profile in the altitude range 5-18 km for all cases. There is a single ISSL approximately half of the time when ice supersaturation is observed anywhere in that altitude, regardless of whether the Appleman criterion is met. When contrailing cases only are considered, there is a single layer 70-80% of the time. As shown in Figure 4, this conclusion seems to be independent of the location. This large proportion of single CISSLs may challenge the random overlap assumptions used in global models studying contrail issues in which the prediction of contrails at one layer are assumed to not affect the presence of contrailing layers above or below.

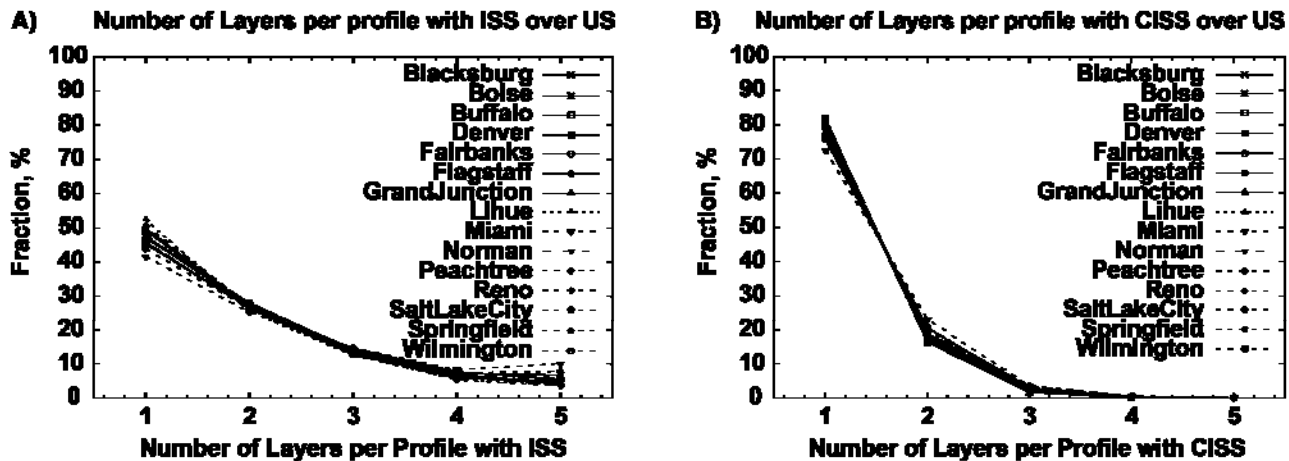


Figure 4. The relative probability as a function of number of ice supersaturated layers without (left panel) and with (right panel) the Appleman criterion over 15 US locations.

Using these results, we can explore how changes in altitude might alter the probability of contrail formation. As an example, we examine the radiosonde data at flight level 350 (35 kft or 10.7 km altitude) for all the sites. For each profile where a contrail would have formed at this flight level, we evaluate the probability distribution of forming a contrail for altitude changes in intervals of  $\pm 1$  kft (the current minimum cruise altitude change that might be considered). This was repeated for each radiosonde location. Figure 5 shows the cruise altitude change as a function of the latitude of the station location in order to reduce the contrail probability by half. The results show that changes of 2-4 kft would have reduced the probability by half for those cases where a contrail would have formed at 35 kft altitude. Note that these results should be used with caution for contrail avoidance,

since our radiosonde measurements do not contain any information about the horizontal extent of CISSLs. In order to avoid contrails in real life we need to know near-real-time RHI fields. So, better data and RHi forecasting techniques would be needed. Our results illustrate that, if contrails must be reduced, a viable option could be to change altitude enroute to fly above or below the CISSL. Although requiring much better humidity data than now exists, this may be a much easier solution rather than designing airplanes and the air space system for new cruise altitudes where contrails would never form.

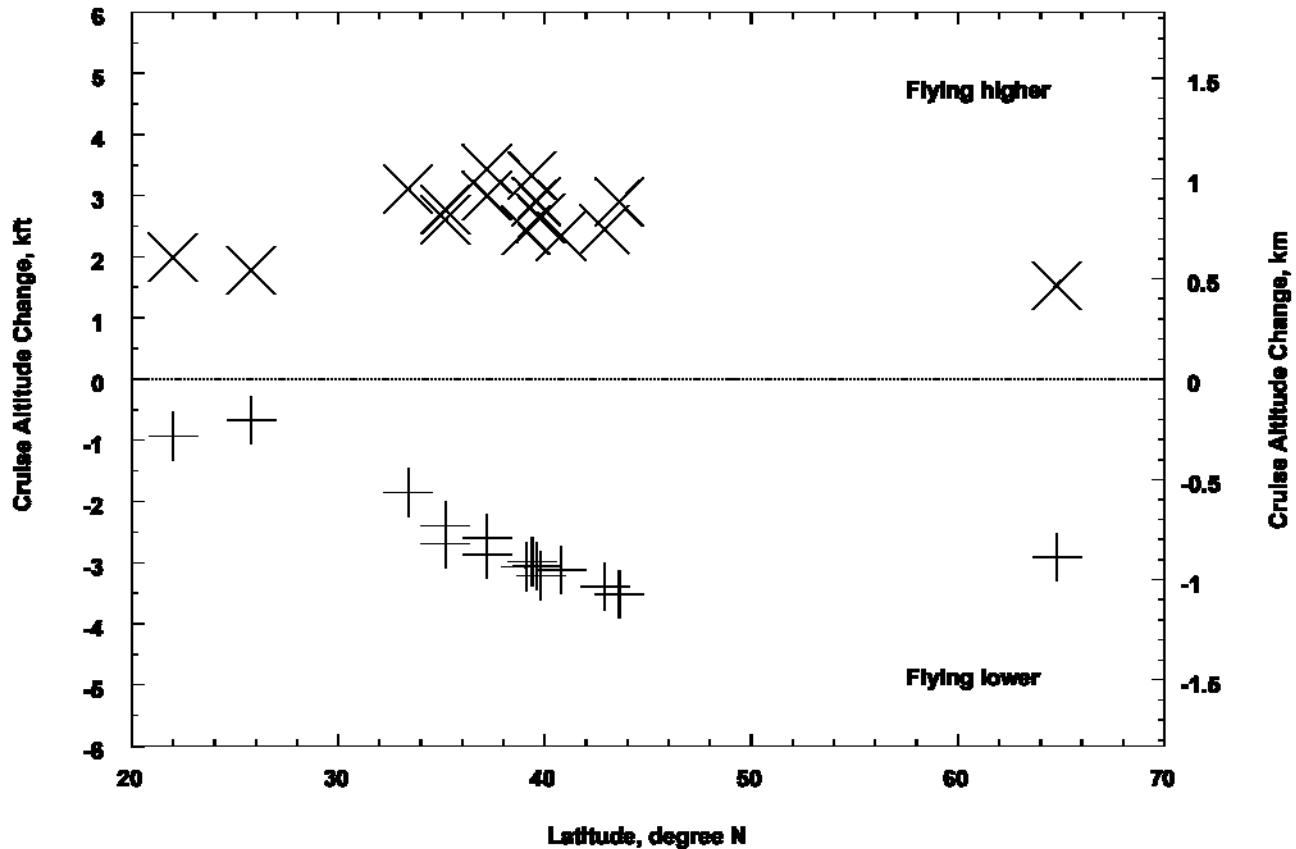


Figure 5. Cruise altitude changes required to halve the persistent contrail formation for flights at flight level 350 (35 kft or 10.7 km altitude) as a function of latitude, for flying higher (X) and for flying lower (+).

#### 4 CONCLUSIONS AND RECOMMENDATIONS

The modified Appleman criterion is important in interpreting ice supersaturated layer (ISSL) results for contrails, particularly at warmer temperatures. Usually only a single ISSL was observed for which a persistent contrail could form. This suggests that random overlap assumptions used in some global models may not correctly predict such behaviour and should be used with caution in evaluating contrail mitigation options. The median contrailing ISSL thickness was found to be 0.7-1.2 km near 9 km altitude dropping to 0.3-0.8 km at 12-13 km altitude. If an aircraft is flying in a contrailing ISSL, changing the flight level by 2-4 kft may reduce the contrail probability significantly.

Much more reliable observational data on relative humidity at multiple cruise altitudes for different locations are needed. Multiple measurements at different altitudes in the same geographical region and for different regions are needed to better constrain atmospheric models and understand mitigation options. Simultaneous measurements of humidity and cirrus properties are needed to better interpret supersaturation events. Better predictive capabilities for RHi in near real time will be needed to identify areas where contrails would form.

## REFERENCES

- Mannstein, H., P. Spichtinger, K. Gierens, 2005: A note on how to avoid contrail cirrus. *Transport. Res. Part D 10*, 421–426.
- Miloshevich, L. M., A. Paukkunen, H. Voemel, and S. J. Oltmans, 2004: Development and validation of a time-lag correction for Vaisala radiosonde humidity measurements. *J. Atmos. Oceanic Technol.*, 21, 1305–1327, doi:10.1175/1520-0426
- Rädel, G, and K. P. Shine, 2007: Evaluation of the use of radiosonde humidity data to predict the occurrence of persistent contrails. *Q.J.Roy.Meteor.Soc.* 133: 1413.1423 DOI: 10.1002/qj.128.
- Schumann, U., 1996: On conditions for contrail formation from aircraft exhausts. *Meteorol. Z.* 5, 4–23.
- Spichtinger, P., K. Gierens, U. Leiterer, and H. Dier, 2003: Ice supersaturation in the tropopause region over Lindenberg, Germany. *Meteorol. Z.* 12, 143–156.
- Wang, J. H., H. L. Cole, D. J. Carlson, E. R. Miller, K. Beierle, A. Paukkunen, and T. K. Laine, 2002: Corrections of humidity measurement errors from the Vaisala RS80 radiosonde - Application to TOGA COARE data. *J. Atmos. Ocean. Tech.*, 19, 981–1002.

# Condensation Trails in the regional Climate Model CCLM

A. Ferrone\*, P. Marbaix, R. Lescroart, J.-P. van Ypersele

*Université catholique de Louvain, Institut d'astronomie et de géophysique G. Lemaître, Louvain-la-Neuve, Belgium*

**Keywords:** Regional Climate Modeling, Contrails, cirrus clouds, aviation climate impacts

**ABSTRACT:** The aviation sector is one of the fastest growing sectors in the world, and its recent inclusion in the EU-ETS aims at limiting the growth of its CO<sub>2</sub> emissions. However this policy does not take into account the non- CO<sub>2</sub> effects of aviation, including the impact of NO<sub>x</sub> on ozone and methane as well as condensation trails (contrails) and their evolution into cirrus clouds, the so-called “aircraft induced cloudiness” (AIC). The regional climate model CCLM is used in order to quantify the impacts of aviation on climate in Europe. A parameterization was added that creates supplementary ice clouds when the mete-orological conditions permit to create contrails and the air is ice-supersaturated. A first test case is performed, which gives an appreciation of the potential AIC over Europe (i.e. it assumed that planes are flying everywhere). This experiment shows that some regions, like the Scandinavian peninsula but also the English Channel and the North-Sea are more prone to form contrails than other. Then a run has been performed based on real flight distributions, which shows that the model is capable of capturing some important patterns that have also been ob-served in observation studies of linear contrails in satellite images.

## 1 INTRODUCTION

Under well defined conditions (see Schumann, 2000) the hot and moist engine exhaust gases of air-planes at cruise level trigger the formation of condensation trails (contrails) in the wake of the aircraft. If the surrounding air is ice-supersaturated these contrails become persistent and transform into cirrus clouds and can persist for several hours (IPCC,1999).

It has been shown (IPCC, 1999, IPCC, 2007) that this so-called aircraft induced cloudiness (AIC) has a warming impact on climate, although the magnitude of the impact is not well deter-mined. This study aims at modeling the contrail formation and their evolution into cirrus clouds with the regional climate model CCLM (Cosmo model in CLimate Mode) over Europe. A regional model has been chosen as its cloud microphysics are generally more detailed than in global climate mod-els. The higher resolution of the model (20km x 20km) permits a more detailed representation of small-scale structures like contrails. The global contrail coverage is spatially very inhomogeneous. Therefore Europe has been chosen as a model domain as it presents very high coverage due to the high traffic density over this region.

First a description of how air-traffic influences the cirrus cloudiness is given, followed by a de-scription of regional model CCLM that is used for this study. Next the parameterization that has been introduced into the model to represent contrails is described and results for the potential con-trail cover and for a case based on real movement data are presented. Finally we will conclude and give an outlook of the project.

## 2 MODEL DESCRIPTION

For this paper the regional climate model CCLM is used, which is based on the numerical weather production model COSMO (formerly LM, see Steppeler et al., 2003) used operationally amongst others by the German Weather Serviced (DWD). An overview of the climate version can be found in Will et al. (2009).

---

\* Corresponding author: Andrew Ferrone, Université Catholique de Louvain (UCL) –Institut d'astronomie et de géophysique Georges Lemaître (ASTR), Louvain-la-Neuve B-1348 Belgium Email: andrew.ferrone@uclouvain.be

The model configuration is similar to the configuration used for the consortial runs of the CLM-Community: The model version is 3.14 with  $0.2^\circ$  resolution and 40 vertical levels on a rotated longitude-latitude grid (140x160 grid points). The domain covers entire Europe, spanning from Iceland tot Northern Greece and Southern Spain to the Northern Tip of the Scandinavian peninsula. At the boundaries the model is forced by NCEP re-analysis (Kistler et al. 2001). The model is run from the year 2005.

We use a two-category and one-moment ice-microphysics in CCLM, with prognostic cloud ice and water vapor mixing-ratios. A detailed description can be found in Doms et al. (2005). As in the present paper the focus is on the high troposphere, where only ice-clouds are present, we will give a short description of the formation and depletion of ice-crystals in the scheme. At very low temperatures, below 248.15 K ice crystals are assumed to form at ice-saturation, whereas at higher temperature, up to 267.15 K it is assumed that water-saturation is needed to condensate crystals, which permits high supersaturation to be reached in the model. Once the initial ice-crystals are formed they can grow by water vapor uptake until the ice-saturation level is reached.

Ice-crystals in the scheme can also be formed by the freezing of supercooled clouds droplets below 236.15 K. The main sink of ice in the high troposphere in the scheme is sublimation, when the air gets ice-subsaturated, with a rate depending on the saturation deficiency. At lower altitudes the autoconversion and collection process are also parameterized in the model.

### 3 PARAMETRIZATION OF AIC IN CCLM

The left-hand side of figure 1 shows the growth of cloud ice in a large eddy simulation (LES) done by Lewellen and Lewellen (2001) for different super saturation value of ambient humidity and for different types of airplanes (two and four reactors). Especially for low supersaturation values an initial decrease in ice content can be seen, which is due to an adiabatic warming as the vortices created by the airplane entail the formed ice crystals to lower altitudes and thus warmer temperatures, followed by an increase of ice mass, as air masses are mixing and water vapour from the surrounding air is being fixed on the initial crystals.

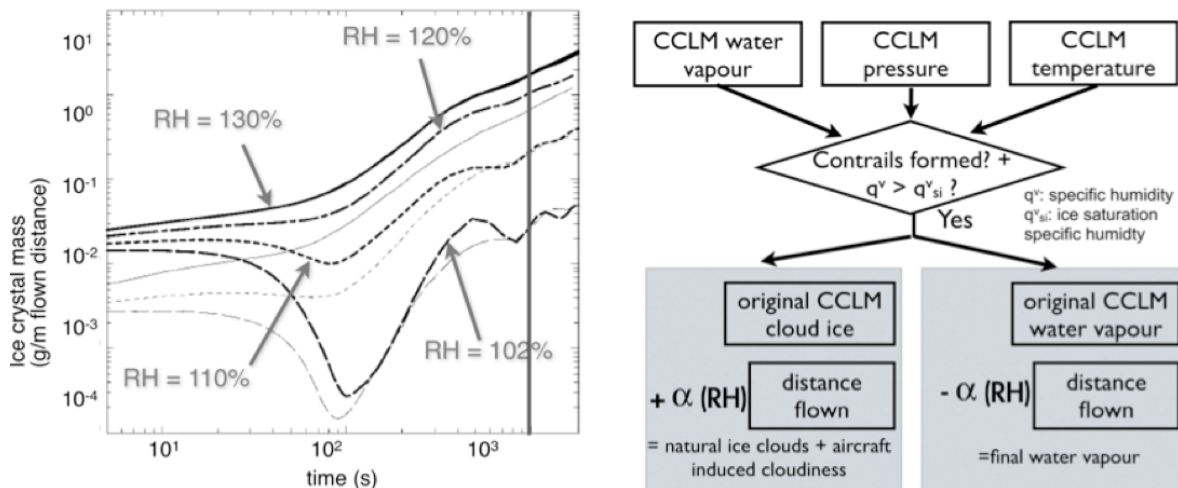


Figure 1: Left side: Ice crystal mass (in g/m of flown distance) as a function of time in the wake of two different types of aircraft, a two-engined one (thin lines) and a four-engined ones (thick lines), done by Lewellen and Lewellen (2001), for different supersaturation values. Right side: Schematic of contrail parametrization introduced in CCLM (see text for description). The parameter alpha is determined by values at 1000 s indicated by the red line on the left graph.

These processes are happening at spatial scales that are not resolved in the climate model. That is why the results of the LES simulation by Lewellen and Lewellen (2001) are introduced in the microphysics of the model if the Appleman-Schmidt criterion is fulfilled and the air is ice-supersaturated (i.e. if persistent contrails are forming). The left side of figure 1 shows that the importance of the supersaturation is an order of magnitude higher than the type of airplane, and in this approach the values given by Lewellen and Lewellen (2001) are linearly interpolated for the different supersaturations, whereas no distinction is made for different airplanes.

As the values in figure 1 are given per flown kilometers, they will be multiplied by the distance flown in the corresponding grid-box. The introduction of the additional ice due to aviation in the microphysics of the model, permits a coherent treatment of the evolution and advection of AIC with natural cirrus clouds and it permits the growth of contrails into cirrus clouds.

## 4 FIRST RUNS WITH THE CONTRAIL PARAMETRIZATION

### 4.1 Runs with homogeneous flight distribution

In order to analyze the differences in the potential to from contrails in different regions a first experiment has been made in which an airplane has been assumed to fly in every gridbox at every timestep. The results thus give us an appreciation of the potential additional cirrus cloud cover due to aviation.

The left-hand side of figure 2, gives the additional high (above 8km) cloud cover in the run with the contrail parametrization and a control run where this parametrization was not used, averaged for 2005. The impact on the high clouds a strong local increase of the cover (up to 5%), which seems to correspond to a recent study done with a GCM that includes the transformation of contrails into cirrus clouds (Burkhardt et al., 2008). This, as well as the difference of magnitude of the direct output of the parametrisation and the additional ice formed after going through the microphysics scheme of the model (see the vertical slices on the right side of figure 2 that follow the black line in the left of figure 2) seem to indicate that the model can simulate the transition from contrails to cirrus clouds. The vertical slices also show that contrails in this case are formed mainly between 8 000 to 12 000 m, which is the altitude at which most supersaturation is observed.

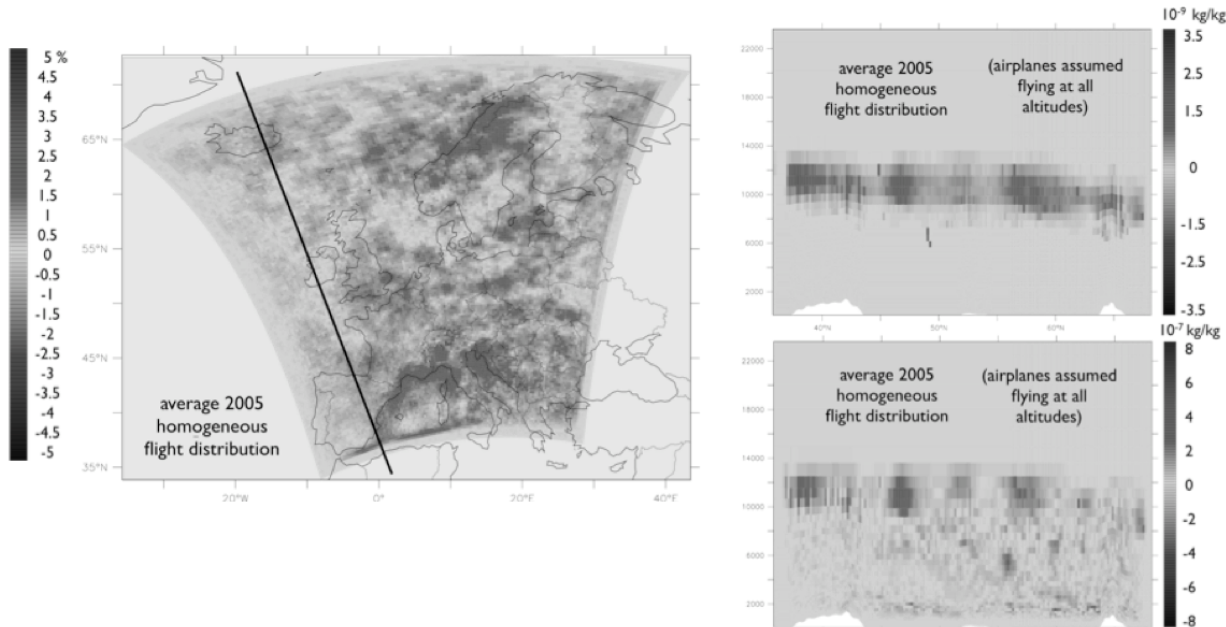


Figure 2 : Left side: Difference of the high cloud cover between a run with contrails and the reference run (in % of coverage) average on 2005, in which airplanes are assumed to fly in every grid box at every timestep, it thus gives a potential contrail cover. Right side: The vertical slices below show the direct output of the contrail parametrisation averaged over 2005 (upper graph, in kg of ice per kg of air) as well as the increase of the ice mixing ratio as a function of altitude (lower graph, in ka of ice, per kg of air)

The increase is higher around the Mediterranean coast and the Scandinavian Peninsula, whereas the North Sea shows a rather low potential to from contrails. In Central Europe, the model shows a high potential over the South of the British Isles, the Channel and the Benelux, whereas Central France and large parts of Germany have a lower potential.

The four graphs on in left-hand side of figure 3 give the evolution of the potential contrail cover averaged over three months for the four seasons. The upper plot on the right side of figure 3 shows the average additional high cloud cover over the region for every month. The potential cover is highest in winter, as the temperatures are very low thus favoring the creation of supersaturation and lowest in June. The lower plot on the right-hand side figure 3 shows the diurnal cycle of the cover-

age, which shows a peak around midday in the annual average. This peak may be related to the onset of convection around this time and can also been seen in the summer average of the diurnal cycle. The predominance of convection with warmer temperatures can also explain the more inhomogeneous distribution of the potential cover in April, May June and July August September in the left side of figure 3.

The upper plot on the right-hand side of figure 3, gives the seasonal evolution of the potential AIC coverage, showing a maximum in winter and a minimum around June. This corresponds to the observed variation of supersaturated areas in this region.

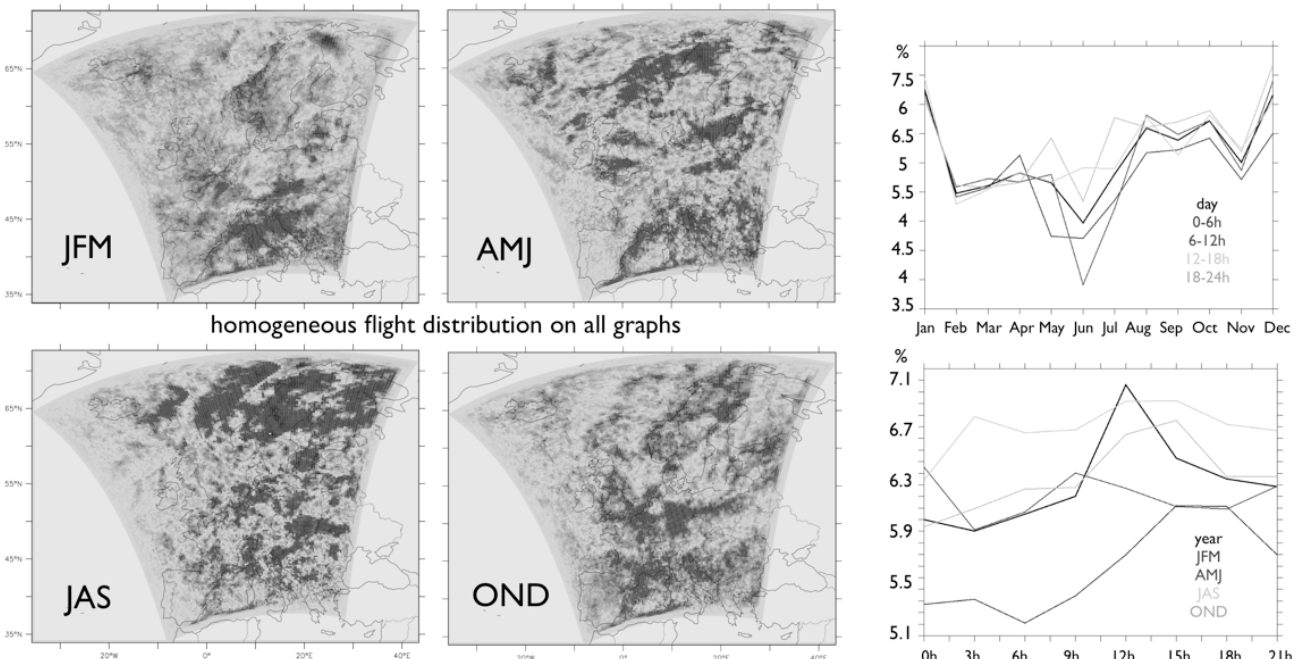


Figure 3: Left side: The four graphs show the evolution of the potential contrail cover averaged over three months (in % of coverage) for January, February March, (JFM), April Mai June (AMJ), July August September (JAS), October, November, December (OND), for the homogenous case (see text). Right side: The upper plot shows the evolution of the average additional high cloud cover over the region as a function of time (in % of coverage) The black line gives the monthly average considering all timesteps. In gray (from darker to lighter gray) only 0-6h (6-12h, 12-18h, 18h-24h) values are considered. The lower plot shows the average of AIC coverage (in % of coverage) as a function of time of day. In black (from darker to lighter gray) the whole year (JFM, AMJ, JAS, OND) is averaged.

#### 4.2 Runs with real flight distribution

One run has been done where the flight distribution over Europe is based on data from the AERO2k database (Eyers et al., 2004). This database gives the flown distance for 2002 on a grid by  $1^\circ \times 1^\circ$  and 500 ft vertical resolution. A first step was to downscale the grid on the model grid, which has a resolution of  $0.2^\circ \times 0.2^\circ$ . The values were uniformly distributed by the area of coverage of the different grid cells, in a way that the sum of distances remains unchanged.

The right hand side of figure 4 shows us the additional high cloud cover (above 8 km) in this case based on real flight distribution. A comparison with figure 2 shows that the pattern is now much more inhomogeneous, and in particular over Northern Europe AIC in the model is much lower, which is due to a reduced flight density over this areas, compared to Central Europe.

The left hand side of figure 4 gives the observed coverage averaged from 2000-2005 of linear contrails from satellite observations by Meyer et al. (2002). We can first see that this coverage is much lower compared to the AIC as given by CCLM, which is as expected. A comparison shows that the model is capable of capturing some important patterns such as the high cover over Western and the lower cover over Eastern part of France. Also the higher cover over the Benelux and the lower cover over Germany is captured. However the high increase over Spain is absent in the model which may be due to the proximity of the boundary data which do not represent supersaturation.

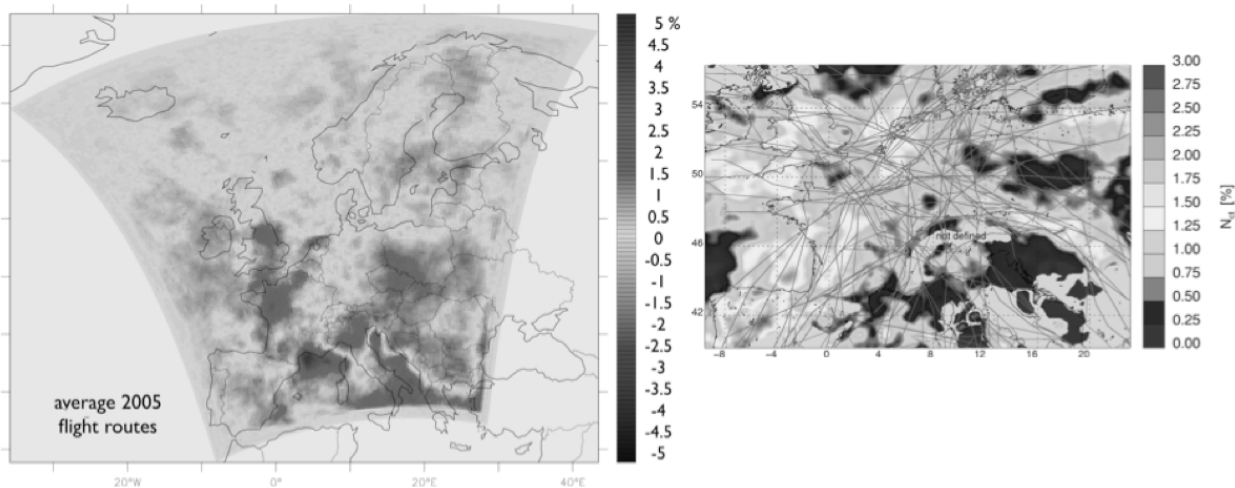


Figure 4 : Left side: Difference of the high cloud cover between a run with contrails and the reference run (in % of coverage) average on 2005, the distribution of flight movements is based on AERO2k (Eyers et al., 2002). Right side: Observation of linear contrail coverage from satellite observations from Meyer et al. (2002).

## 5 CONCLUSION AND OUTLOOK

This first investigation of aircraft induced cloudiness with the regional climate model CCLM shows that the model is able to reproduce some characteristic patterns of contrail coverage. The seasonal and diurnal cycle reproduced by the model is also in accordance with observed evolution of ice-supersaturated regions in the considered region.

The impact on the high clouds shows a strong local increase of the cover (up to 5%), which seems to correspond to a recent study done with a GCM that includes the transformation of contrails into cirrus clouds (Burkhardt et al., 2008).

This, as well as the difference of magnitude of the direct output of the parametrisation and the additional ice formed (see vertical slices) seem to indicate that the model can simulate the transition from contrails to cirrus clouds.

Although these first runs show encouraging results a detailed validation of the simulated contrail coverage and the supersaturation in the model is still to be done.

Next steps of the project will be to perform sensitivity studies (e.g. of the calibration factor  $\alpha$  in the parametrisation and of flight altitude), followed by impact studies of contrails on, for example, the diurnal temperature range, the cloud radiative forcing, the total cloud cover (including low level clouds) and the solar insulation.

## 6 ACKNOWLEDGMENTS

A. Ferrone is supported by the Belgian National Fund for Industrial and Agricultural (FRIA). P. Marbaix and B. Matthews are supported by the Belgian Science Policy Office through the project Aviation and the Belgian Climate Policy: Integration Options and Impacts (Science for a sustainable development SD/CP/01A)

## REFERENCES

- ABCi: W. Hecq, S. Meyer, J. Van Mierlo, J. Matheys, C. Macharis, T. Festraets, J.P. van Ypersele, A. Ferrone, P. Marbaix, B. Matthews, Aviation and the Belgian Climate Policy: Integration Options and Impacts: Final report, phase I, Belgian Public Planning Service Science Policy Rue de la Science 8 - Wetenschapsstraat B-1000 Brussels 87p., 2008
- Burkhardt, U., B. Kärcher, M. Ponater, K. Gierens, and A. Gettelman , Contrail cirrus supporting areas in model and observations, Geophys. Res. Lett., 35, L16808, doi:10.1029/2008GL034056, 2008

- Doms, G. and Forstner, J.: Development of a kilometer-scale NWP system: LMK, COSMO Newsletter, 4, 159–167, 2004
- Eyers C., P. Norman, J. Middel, M. Plohr, S. Michot, and K. Atkinson, AERO2k Global Aviation Emissions Inventories for 2002 and 2025, 2004
- IPCC: J. E. Penner, D. H. Lister, D. J. Griggs, D. J. Dokken, and M. McFarland, editors, *Aviation and the Global Atmosphere*, Cambridge University Press, Cambridge, United Kingdom and New York, NY, USA, 1999
- IPCC: S. Solomon, D. Qin, M. Manning, Z. Chen, M. Marquis, K. Averyt, M. Tignor, and H. Miller, editors, *Climate Change 2007: The Physical Science Basis. Contribution of Working Group I to the Fourth Assessment Report of the Intergovernmental Panel on Climate Change*, Cambridge University Press, Cambridge, United Kingdom and New York, NY, USA, 2007
- Kistler, R., E. Kalnay, W. Collins, S. Saha, G. White, J. Woollen, M. Chelliah, W. Ebisuzaki, M. Kanamitsu, V. Kousky, H. van den Dool, R. Jenne, and M. Fiorino: The NCEP-NCAR 50-Year Reanalysis: Monthly Means CD-ROM and Documentation. *Bull. Amer. Meteor. Soc.*, 82, 247–268, 2001
- Lee, D.S., D.W. Fahey, P.M. Forster, P.J. Newton, R.C.N. Wit, L.L. Lim, B. Owen, and R. Sausen, Aviation and global climate change in the 21<sup>st</sup> century, *Atmospheric Environment*, doi: 10.1016/j.atmosenv.2009.04.024, 2009
- Lewellen D. C. and W. S. Lewellen, The effects of aircraft wake dynamics on contrail development, *Journal of the Atmospheric Sciences*, 58(4), pp. 390–406, 2001
- Meyer R., H. Mannstein, R. Meerkötter, P. and Wendling, Contrail and cirrus observations over Europe from 6 years of NOAAAVHRR data, *EUMETSAT Meteorological Satellite Conference*, edited by EUMETSAT, vol. EUM P 36, pp. 728–735, 2002
- Sausen R. and I Isaksen and V. Grewe and D. Hauglustaine and D. S. Lee and G. Myhre and M. O. Köhler and G. Pitari and U. Schumann and F. Stordal and and C. Zerefos, 2005. Aviation radiative forcing in 2000: An update on IPCC. *Meteorologische Zeitschrift*, Vol. 14, 555–561, 2000
- Schumann U., Influence of propulsion efficiency on contrail formation. *Aerosp. Sci. Technol.*, 4(6), pp. 391–401, 2000
- Steppeler, J., Doms, G., Schättler, U., Bitzer, H.W., Gassmann, A., Damrath, U., Gregoric, G., Meso-gamma scale forecasts using nonhydrostatic model LM, *Meteorological Atmospheric Physics*, 82, 75–96, 2003
- Will A., M. Baldauf, B. Rockel, A. Seifert, Physics and Dynamics of the COSMO-CLM, *Meteorol. Z.*, submitted, 2008

# Some evidence of aviation fingerprint in diurnal cycle of cirrus over the North Atlantic

K. Graf\*, H. Mannstein, B. Mayer, U. Schumann

Deutsches Zentrum für Luft- und Raumfahrt, Institut für Physik der Atmosphäre, Oberpfaffenhofen, Germany

*Keywords:* Contrail, Contrail Cirrus, Aviation

**ABSTRACT:** The diurnal cycle of aviation in the North Atlantic Region (NAR; 45° W – 10° W, 45° N – 55° N) shows a unique fingerprint dominated by two maxima due to rush-hours in west-bound resp. eastbound air traffic. We investigate the hypothesis that this signature can be found also in the diurnal cycle of cirrus coverage. Air traffic data were kindly provided by EUROCONTROL with adequate temporal and spatial resolution for this investigation. The cirrus cover is derived from Meteosat-8/9 SEVIRI data with a spatial resolution of about 5 km and a temporal resolution of 15 min using the cirrus detection algorithm MeCiDA (Krebs et al., 2007). Aviation induced cloud cover changes are derived from diurnal cycle of cirrus cover observed in NAR. We developed several response functions representing the effect of air traffic on cirrus coverage and applied fitting methods for determination of the fit parameters representing the statistical lifetime and the amount of AIC in NAR. Application of the fitting procedures to the air traffic density (ATD) allows us to reproduce the signature of cirrus coverage observed in cirrus coverage. The results are robust for investigations of sub regions of NAR with different signatures of initial ATD and shifts in the occurrence of maxima. Several satellite scenes illustrate the statistical behaviour in single scenes.

## 1 DATASETS – CIRRUS COVERAGE AND AIR TRAFFIC DENSITY

The MSG cirrus detection algorithm MeCiDA (Krebs et al., 2007) using seven infrared channels of MSG-SEVIRI is applied, delivering a time series of cirrus coverage for the considered region with a temporal resolution of 15 minutes.

---

\* Corresponding author: Kaspar Graf, Deutsches Zentrum für Luft- und Raumfahrt, Institut für Physik der Atmosphäre, Oberpfaffenhofen, Germany. Email: Kaspar.Graf@dlr.de

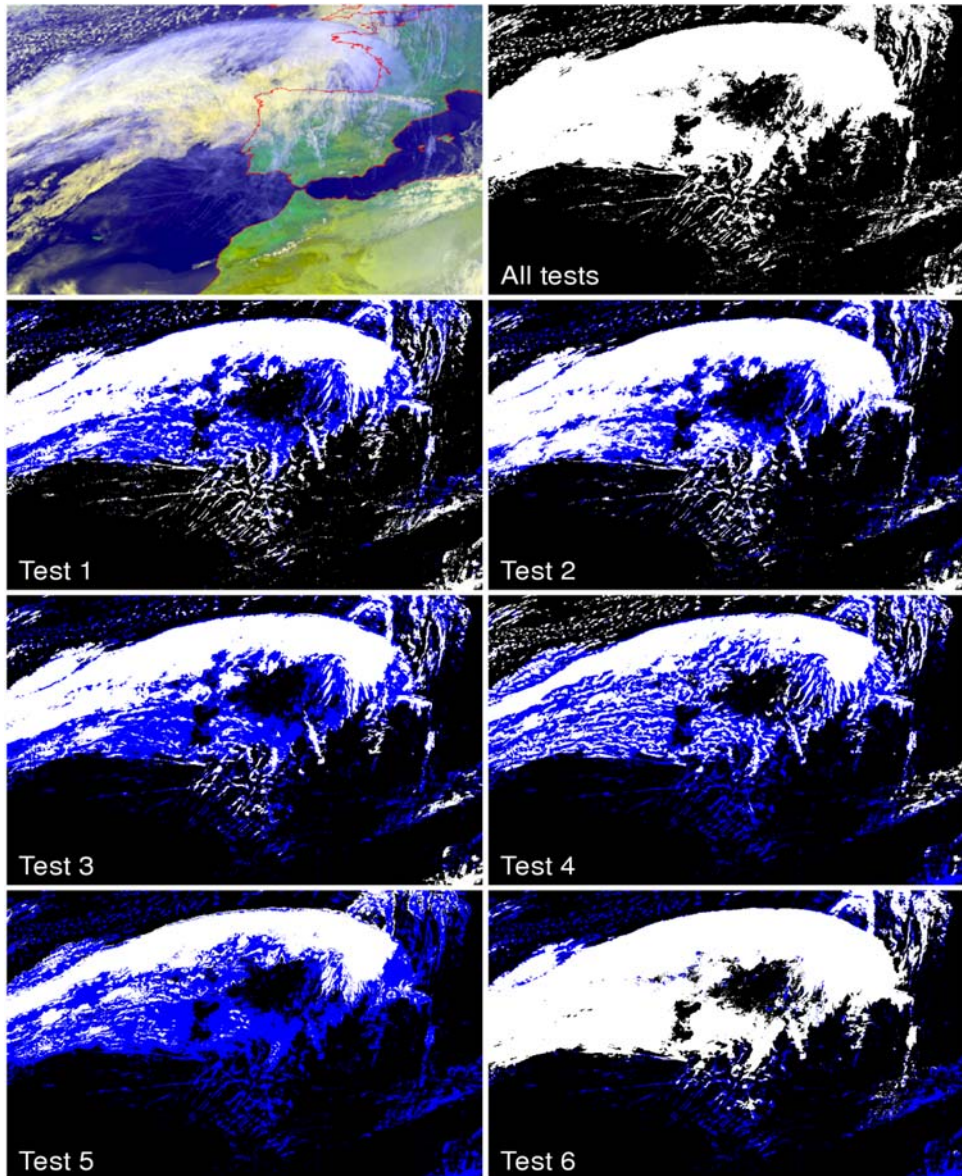


Figure 1. Top left: False color composit of an exemplary cirrus scene. Top right: MeCiDA cirrus classification. The resulting cirrus classification is a combination of six individual cirrus tests which are combined by a logical “OR”, see Krebs et al. (2007).

Based on this time series the diurnal cycle of cirrus coverage in NAR can be obtained. Missing time steps (e.g. satellite malfunction) are interpolated. The diurnal cycle for several sub regions of NAR is determined similarly. The algorithm was applied to a four year time period (02/2004 –01/2008). Within the ESA-DUE Project CONTRAILS, EUROCONTROL provided a dataset of air traffic density (ATD) for six weeks in 2004 with a temporal resolution of 15 min and a spatial resolution of  $0.25^\circ \times 0.25^\circ$  for the region shown in figure 2.

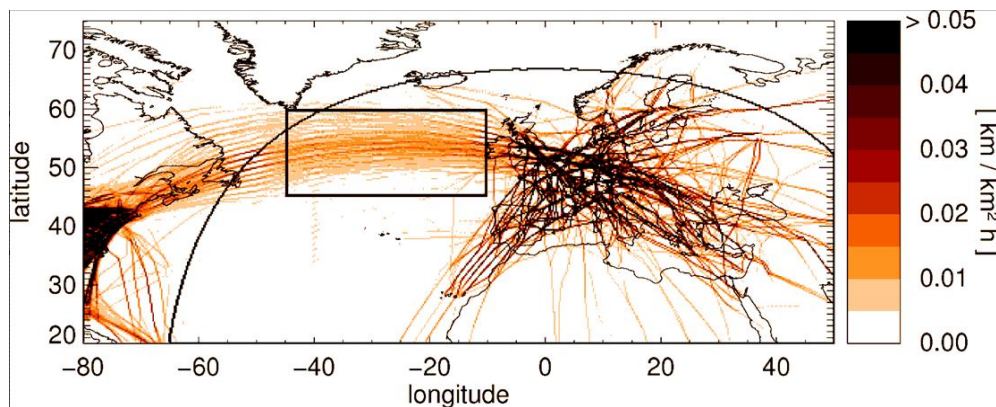


Figure 2. Mean air traffic density in Europe and the North Atlantic. The region NAR is marked by the box. The curve is representing the  $75^\circ$  satellite zenith angle of Meteosat-8/9.

This dataset allows the determination of a representative diurnal cycle of ATD in the NAR, showing a peak at 4 am (UTC) representing the eastbound transatlantic rush hour whereas the peak at 4 pm represents the maximum in westbound traffic.

## 2 METHOD

The mean diurnal cycle of cirrus coverage shows a pattern similar to a delayed ATD diurnal cycle.

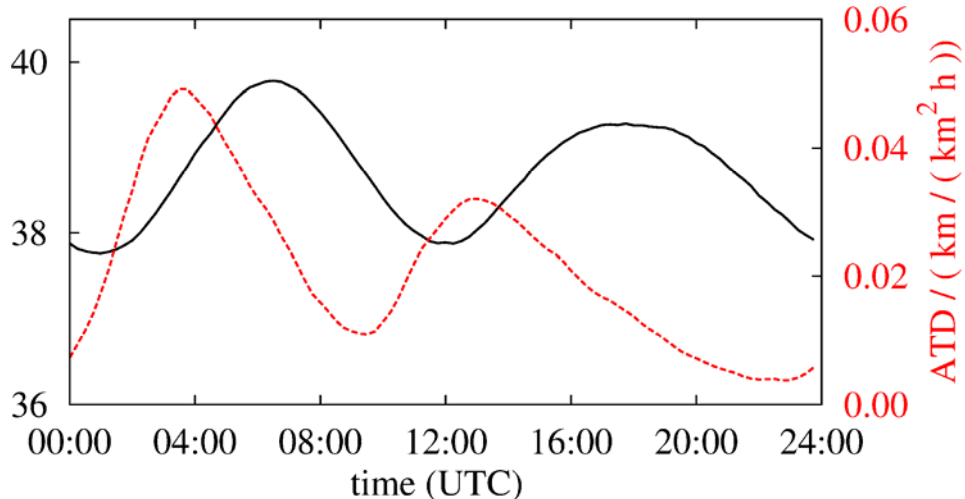


Figure 3. Mean diurnal cycle of air traffic density in NAR (red) and observed cirrus coverage in the same region (black) for 2004.

The diurnal cycle of cirrus coverage can be described as a composite of a constant background, a natural diurnal cycle and an AIC component:

$$C(t) = C_{mean} + C_0(t) + c_{AIC}(t)$$

The natural diurnal cycle  $C_0(t)$  is either assumed to be negligible or assumed to be identical to the one observed in the corresponding South Atlantic Region SAR. The AIC contribution to the cirrus cover at time  $t$ ,  $c_{AIC}(t)$  can be expressed statistically as a superposition of all air traffic events in the past,

$$c_{AIC}(t) = \int_{-\infty}^t a(t') \cdot r(t-t') dt',$$

where  $r$  is representing the mean AIC at time  $t$  triggered by an air traffic event at time  $t'$ . For quantification of AIC, we use several response functions  $r(t)$  representing this answer of cirrus cover to an air traffic event:

$$r_1(t) = s \cdot \delta(t-\tau), \quad \delta(t) = 0 \text{ for } t \neq 0, \quad \int_{-\infty}^{\infty} \delta(t) dt = 1$$

$$r_2(t) = \begin{cases} s \cdot t \cdot e^{-\lambda \cdot t} & \text{for } t \geq 0 \\ 0 & \text{for } t < 0 \end{cases}$$

$$r_3(t) = b \cdot t^c \cdot e^{-d \cdot t} \cdot e^{-f \cdot t^2}$$

$$r_4(t) = b \cdot t^c \cdot e^{-d \cdot (t-f)^g}$$

Based on the ATD, the coefficients of the response functions are least-square-fitted to the cycle in cirrus coverage (see Fig. 4)

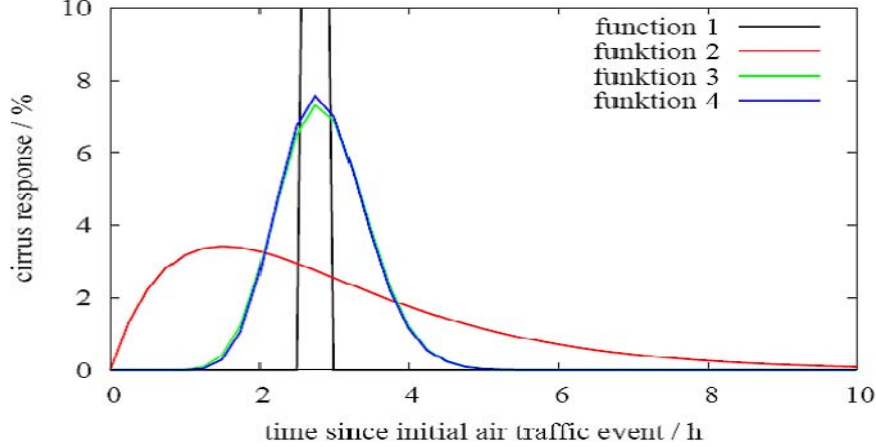


Figure 4. Shape of the different response functions declared in the text.

### 3 RESULTS

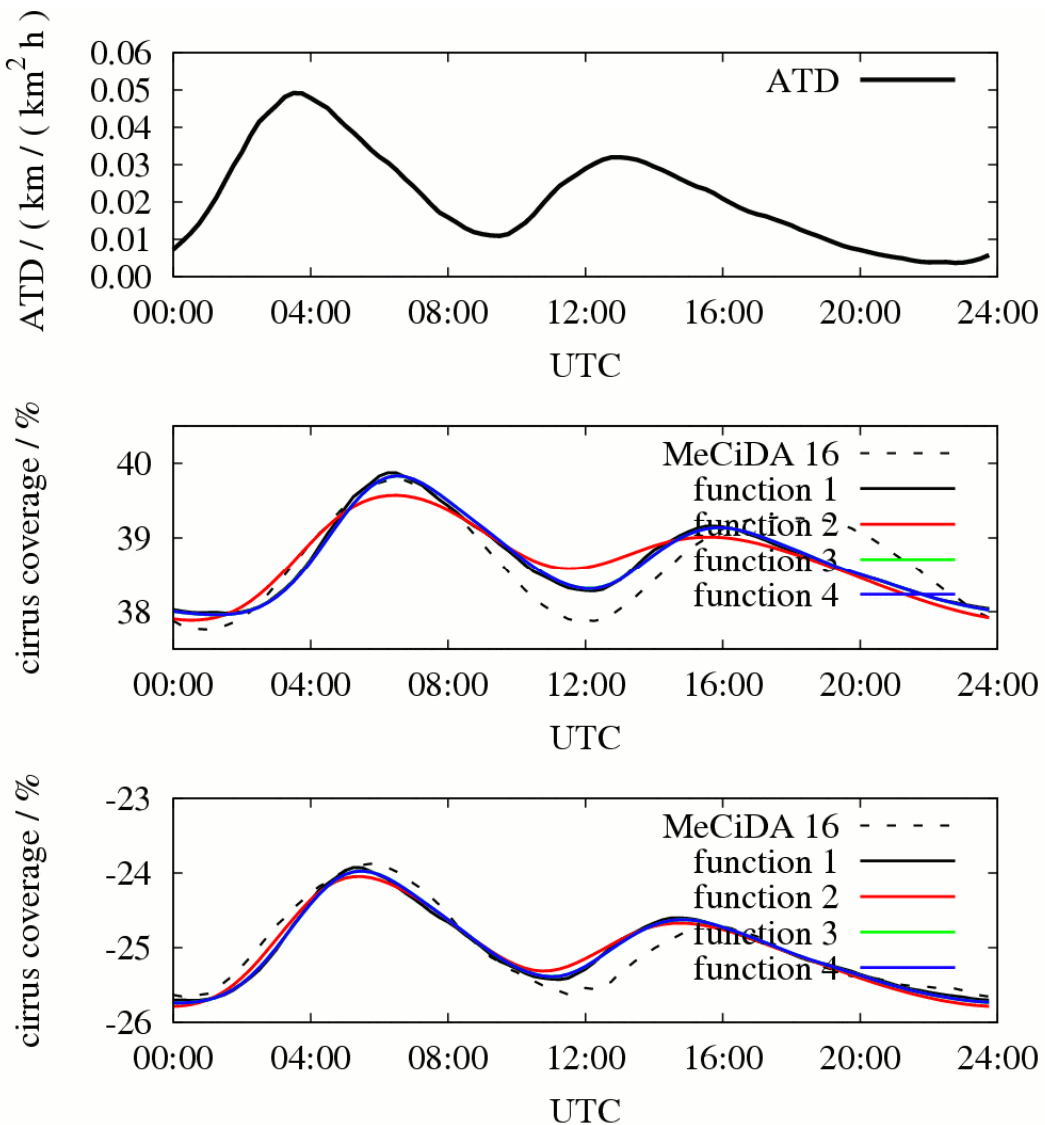


Figure 5. Diurnal cycle of ATD in NAR, based on six weeks in 2004 (top), observed and fitted diurnal cycle of cirrus coverage for the cases  $C_0(t) = 0$  (middle) and  $C_0(t) = C_{SAR}(t)$  (bottom).

On figure 5, the fitting results based on the ATD input (top) are shown for the case  $C_0(t) = 0$  (middle) and  $C_0(t) = C_{SAR}(t)$  (bottom). It is obvious that the fitting result is different for each response function. In general, the fitting procedure performs better for the case  $C_0(t) = C_{SAR}(t)$ .

Table 1. Fitting results for response functions  $r_1$ ,  $r_2$ ,  $r_3$  and  $r_4$  as declared in the text.

nr	$C_0(t)$	$C_{\text{Mean}}$	s	$\tau$ in h	-	-	-	$\rho$	$\Delta c$	$c_{\text{AIC}}$
1	0	0.378	0.416	2.75	-	-	-	0.871	0.003	0.0083
1	SAR	-0.259	0.392	1.75	-	-	-	0.946	0.017	0.0083
			s	$\lambda$	-	-	-			
2	0	0.375	0.061	0.66	-	-	-	0.790	0.0038	0.0119
2	SAR	-0.26	0.145	1.11	-	-	-	0.940	0.0019	0.0098
			b	c	d	f	-			
3	0	0.378	0.0044	7.05	0.345	0.71	-	0.867	0.0031	0.0095
3	SAR	-0.259	0.0864	2.89	0.428	0.39	-	0.949	0.0017	0.0089
			b	c	d	f	g			
4	0	0.378	0.5605	17.39	1.50	2.25	1.60	0.870	0.0031	0.0092
4	SAR	-0.259	3.7676	4.51	1.10	1.61	1.48	0.949	0.0017	0.0089

The fit parameters are shown in table 1. For fit function 1 (simple delay), best fits are obtained for a time shift of 1.75 resp. 2.75 h. The 24-h mean AIC in NAR is 0.83% in both cases. For the other response functions, AIC amounts to about 0.8 – 1.2%, depending on which assumption for  $C_0(t)$  is used. All results shown here are based on data from February – December 2004, as for the following years no representative ATD dataset is available so far.

#### 4 CONSISTENCY

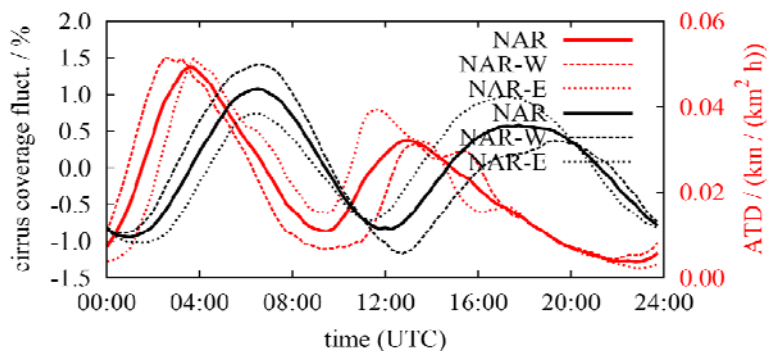


Figure 6. Diurnal cycle of ATD (red) and cirrus coverage (black) for the sub regions NAR-W and NAR-E, the western resp. eastern part of NAR.

The peak representing ATD in eastbound direction occurs earlier in the western part of NAR than in the eastern one, whereas the westbound peak occurs earlier in the eastern part of the NAR. This unique (i.e. non-meteorological) behaviour can be retrieved in the cirrus coverage as well (Fig. 6).

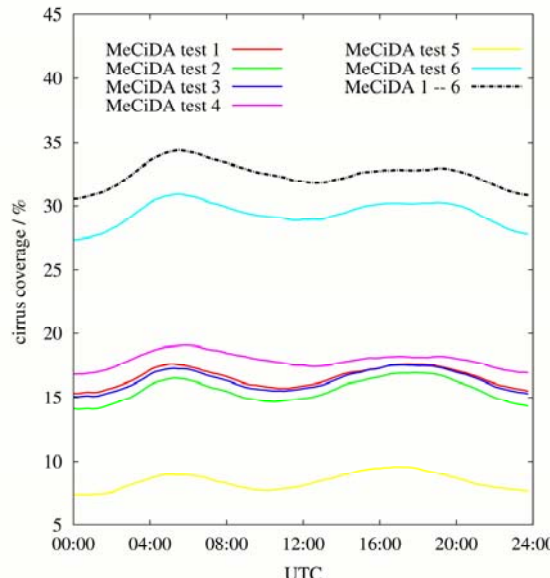


Figure 7. Diurnal cycle of cirrus coverage derived by the six individual cirrus tests of MeCiDA for NAR, 2004.

MeCiDA consists of six individual cirrus tests based on different channel combinations of MSG-SEVIRI. These tests are combined by a logical “OR”. Applying each test alone to a data-subset, the diurnal cycle in cirrus coverage is consistent with the total MeCiDA result (see figure 7). Therefore, artefacts due to a “diurnal-cycle sensitive” channel (e.g. the ozone channel 9.3  $\mu\text{m}$ ) are excluded. Furthermore, periodic oscillations of MSG around its nominal position were analysed. The frequency of these oscillations would not cause a diurnal cycle.

## 5 EXAMPLE AND OUTLOOK

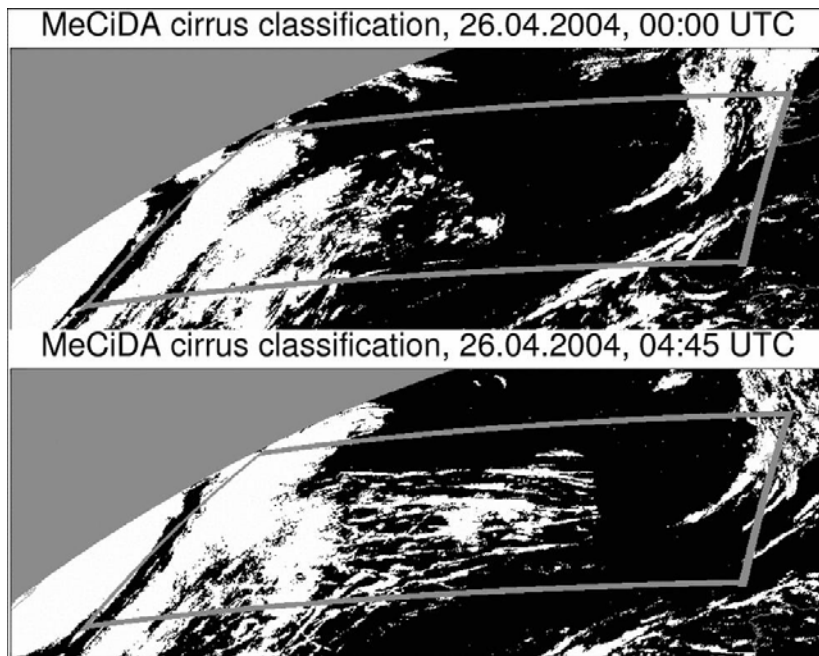


Figure 8. Cirrus scenes derived with MeCiDA.

The visibility of AIC in satellite data is illustrated by the two scenes shown in figure 8: At 0:00 UTC, ATD is low and the last peak was 10 hours ago. Therefore, no significant ATD fingerprints are visible in the satellite scene. At 4:45 UTC, the westbound ATD has passed the region two hours ago and triggered AIC in the NAR. In the following time, this AIC is decreasing until the eastbound ATD triggers new AIC formation. Further work is needed for a better identification and understanding of natural contributions in diurnal cycle of cirrus coverage in NAR as well as SAR.

The HALO campaign “ML-CIRRUS” will address the validation of diurnal cycle in AIC. So far, analysis is based on an ATD dataset of several weeks. A complete ATD dataset is needed for a more detailed consistency check and for comparisons with the Contrail and Cirrus Prediction tool CoCiP (Schumann, 2009).

## 6 ACKNOWLEDGEMENT

We thank S. Rentsch for data handling support. Meteosat 8/9 data were provided by EUMETSAT via the German Sensing data center at DLR and air traffic data were provided by EUROCONTROL, both within the ESA-DUE project CONTRAILS. The work performed was part of the DLR projects PAZI 2 and CATS, and the BMBF project UFO within Klimazwei.

## REFERENCES

- Krebs, W., H. Mannstein, L. Bugliaro, and B. Mayer, 2007, Technical note: A new day- and night-time Meteosat Second Generation Cirrus Detection Algorithm MeCiDA. *Atmos. Chem. Phys.*, 7, 6145-6159  
 Schumann, U., 2009: A Contrail Cirrus Prediction Tool. In: Sausen, R. et al. (eds.): Proceedings of an International Conference on Transport, Atmosphere and Climate (TAC-2). Aachen, Maastricht, 2009, in press

# Aviation and ship soot as freezing nuclei of water/sulfate cloud droplets

E. Kireeva\*, O. Popovicheva, N. Persiantseva  
*Institute of Nuclear Physics, Moscow, Russia*

N. Shonija, T. Khokhlova  
*Dept. of Chemistry, Moscow State University, Moscow, Russia*

**Keywords:** immersion freezing nucleation, soot aerosols, aviation and ship emission

**ABSTRACT:** Laboratory study of heterogeneous freezing of water/sulfate droplets induced by immersed aviation and ship soot particles is reviewed. In order to identify the impact of individual transport soot particles on the droplet freezing efficiency a set of well-characterized laboratory soots with different properties are analyzed along with aviation and ship soots. This laboratory approach allows the identification of the properties for the most effective immersion freezing nuclei. The maximum temperature shift due to heterogenous freezing in respect to homogeneous freezing is found to be 10°C for hydrophobic soot immersed into sulfuric acid solution droplets. Aviation and ship – emitted aerosols cannot be referring as effective immersions freezing nuclei in both water and sulfuric acid droplets due to high hygroscopicity and water soluble fraction on their surface.

## 1 INTRODUCTION

The major source of uncertainties in assessing aerosol indirect effects on climate is the emission of soot aerosols. Transport - emitted aerosols may act as effective ice nuclei impacting the Earth's climate indirectly by changing the properties and lifecycle of clouds. The commonly observed carbon-containing particles in cirrus ice crystals indicate that aerosol particles can stimulate the process of ice formation in the atmosphere. It is assumed that aerosols after the evaporation of contrail ice crystals can change the microphysical properties of cirrus clouds (Strom and Ohlsson, 1998). Heterogeneous ice formation in cirrus clouds due to immersed soot aerosols can occur at noticeably lower degrees of water supersaturation than those required for the homogeneous formation of sulfate aerosols (DeMott et al., 1997).

However, the effects of aviation and ship soot emission on freezing the cloud droplets along with the mechanism that could lead to heterogeneous ice nucleation by soot particles at the cirrus level are not clear. The field observations of transport emission particulates and their influence on freezing ability are much limited because of the great difficulties in direct measurements of soot aerosols involved in ice cloud formation. This situation is complicated by the fact that soot particles emitted into atmosphere from aircrafts and ships have a wide range of a natural variability with respect to physico-chemical properties including the composition and extent of hygroscopicity. Laboratory approach can provide relevant information to establish the link between physico-chemical properties of soot particles and their freezing activity.

This work is devoted to laboratory studies of heterogeneous freezing of water and sulfate droplets induced by immersed soot. Along with original transport soot (aviation and ship residuals) a set of well-characterized laboratory soots with various extent of hygroscopicity is investigated. The median freezing temperature of an ensemble of water and sulfate droplets with soot immersed demonstrates a clear impact of soot wetting, hydrophilicity, and water soluble fraction. The characteristics of soot particles active in the immersion freezing mode are thereby suggested. The efficiency of

---

\* Corresponding author: Elena Kireeva, Institute of Nuclear Physics, Moscow, Russia. Email: elenakireeva2@gmail.com

aviation and ship soot as freezing nuclei in water/sulfate cloud droplets in the atmosphere is reported.

## 2 EXPERIMENTAL SECTIONS

### 2.1 Aviation and ship soot sampling

A sampling campaign for monitoring a number of seagoing transport ships was undertaken in the framework QUANTIFY EU project in the Odessa port. Ship emitted particulates were collected during a few months onboard of a diesel-powered marine tanker using distillate diesel oil fuel. A high-volume bulk aerosol sampler mounted at the ship end-of-pipe was used. Diesel fuel typically contained not more than 0.5% of sulfur and 0.01% of ash. Aircraft engine combustor (AEC) soot was produced by a combustor of a modern gas turbine engine, model D30-KU, operating at cruise combustion conditions on a test facilities in CIAM, Moscow (Popovicheva et al., 2004). The engine fuel was aviation kerosene TC1 containing 0.11 % of sulfur and less than  $10^{-4}$ % of metals.

### 2.2 Immersion freezing experiments

Detailed description of freezing experiment is given in Popovicheva 2008. To obtain statistically reliable data the freezing of an ensemble of 100 microdroplets of 0.13 cm was examined in a cooled cell. For preparation of the soot suspensions the agglomerates of the size less than 80  $\mu\text{m}$  was used; a particle number density in the microdroplets was 2.5 wt %. As a measure of the freezing efficiency a difference between the median freezing temperature of an ensemble of pure microdroplets and ones from soot suspensions,  $\Delta T_f$ , was assumed.  $\Delta T_f$  for pure water droplets and 10 wt% sulfuric acid solution droplets was obtained  $-11.5 \pm 2.1^\circ\text{C}$  and  $-21 \pm 2.5^\circ\text{C}$ , respectively. A set of well-characterized soots with different properties, water-soluble fraction and extent of hygroscopicity were analyzed. It includes lamp soot (LS), furnace black (FB), thermal soot (TS), Printex, and acetylene black (AB) which were produced by combustion of liquid fuel in a lamp and furnace, by the pyrolysis of natural gas and by explosion of acetylene, respectively.

## 3 FREEZING OF WATER DROPLETS WITH SOOT IMMERSED

### 3.1 Soot behaviour in water

The key physical characteristic impacting the water droplet freezing efficiency is the soot particle distribution in water that is influenced by the mass density and size of soot agglomerates, and wetting characteristics. In the case of soot particles of high mass density, like FB soot, the sedimentation instability (see fig.1a) limits the freezing efficiency of droplets. AB soot with a low mass density creates the sedimentation stable suspension with particles homogeneously distributed over droplet volume; these particles have the property of floating and water droplets with AB soot are uniformly dark (see fig.1b). The sedimentation stable water/soot suspensions with homogeneously distributed over droplet volume particles provide the appreciable freezing efficiency, near  $4.7^\circ\text{C}$ . Moreover, there is a correlation between wetting ability of the soot surface and the floating properties of soot agglomerates. For a given mass density, soot characterized by a smaller contact angle is more wettable and therefore its particles more easily sediment on the droplet bottom. It is found that the wettability of soot is in good correlation with their hygroscopicity which is determined from water adsorption isotherms (Persiantseva et al., 2004).

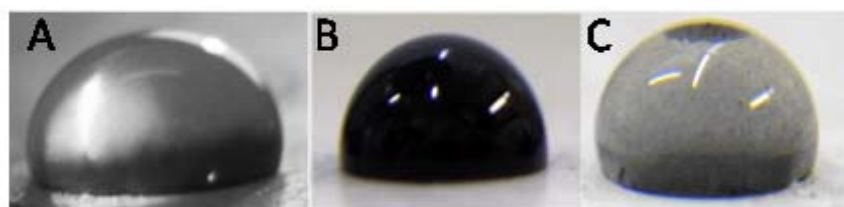


Figure 1. Water droplets with different soot behavior: a) sedimentation instable droplet of FB soot, b) sedimentation stable droplet of AB soot, c) AEC soot droplet with two separated fraction of particles.

Aviation and ship soots have the highest mass density, their particles are partly deposited on the droplet bottom or concentrate at the top (see fig. 1c). This distribution over the droplet is in accordance with findings that aviation soot contains two fractions, one is hydrophobic and other is hydrophilic because of the large amount of water-soluble impurities (Popovicheva et al., 2004).

### 3.2 Extent of soot hygroscopicity and freezing efficiency

Adsorption of water vapor is a sensitive tool to establish the link between the freezing mechanism and soot surface hydration characteristics. Therefore in this work the water uptake as a function of the relative humidity is measuring by a gravimetical method to identify the extent of soot particle hygroscopicity. The fundamental theory of water adsorption on soots assumes that, due to low dispersion energy between water molecules and graphite platelets, there is a strong dependence on the presence of hydrophilic sites, so called primary adsorption sites (oxygen-containing active sites). It is assumed that sites of the adsorption of water molecules are also sites for ice formation. So, the extent of soot hydrophilicity is the second key characteristics relating to immersion freezing efficiency. Our study shows the strong correlation between the numbers of oxygen containing active sites on the soot surface and the freezing efficiency of water droplets with soot immersed.

Hydrophobic particles of TS soot consist mainly from elemental carbon with negligible number oxygen-containing sites. These particles do not promote ice nucleation in the immersion freezing mode. Fig. 2A shows the freezing frequency of pure water droplets versus droplets with TS soot immersed. There is a negligible shift,  $0.4^{\circ}\text{C}$ , in the freezing temperature in respect to pure water droplets (see Table 1).

Table 1. Freezing efficiency ( $\Delta T_f$ ) of droplets with soots immersed and soot water soluble fraction (WSF).

Soots	$\Delta T_f$ of water droplets, $^{\circ}\text{C}$	$\Delta T_f$ of sulfate droplets, $^{\circ}\text{C}$	WSF, %
Ship soot	0.2	2	18
Aviation (AEC) soot	0.9	4	13.5
Furnace Black (FB)	4.2	7.2	0.1
Lamp soot (LS)	3.9	6.5	0.4
Thermal soot (TS)	0.9	6	0.5
Printex		8.8	0.1

The maximum freezing efficiency is about  $4.2^{\circ}\text{C}$  was obtained for FB soot. This soot contains a significant number of oxygen-containing functional groups but not covered totally by hydrophilic sites and soluble compounds. Therefore, a relatively low polar surface is preferable for the ice formation as compared with polar surfaces on which the dipoles of water molecules are predominantly oriented in parallel with one another, thus enhancing the free energy of new phase nuclei formation. Hence, hydrophilic soot is preferable for heterogeneous ice formation. The similar freezing efficiency of  $3.9^{\circ}\text{C}$  was observed for LS soot with the same extent of hygroscopicity (Table 1).

However, if the soot surface contains the high water-soluble inorganic/organic fraction (the case of hygroscopic soots) the active sites may be sensible to dissolution after the particle has become immersed into water. Soluble coverage changes the mechanism of water uptake from water cluster growth on the active sites to the dissolution into soluble surface material. Then, we may predict the reduction of potential ice nucleation ability for really hygroscopic soot.

Both aviation and ship soots are characterized by high water soluble fraction, 13.5% and 18% respectively. Additionally, the WSF of aviation soot contains 3.5 wt% of sulfates which are easily washed by water. Such high WSF leads to extremely high water uptake up to 40 and 500 water monolayers for aviation and ship soots, respectively (Popovicheva et al., 2004; 2009). And therefore the freezing efficiency of these soots are not exceed  $0.9^{\circ}\text{C}$  (Table 1). The histogram of freezing frequency of water droplets with ship soot immersed confirms this finding (fig. 2A).

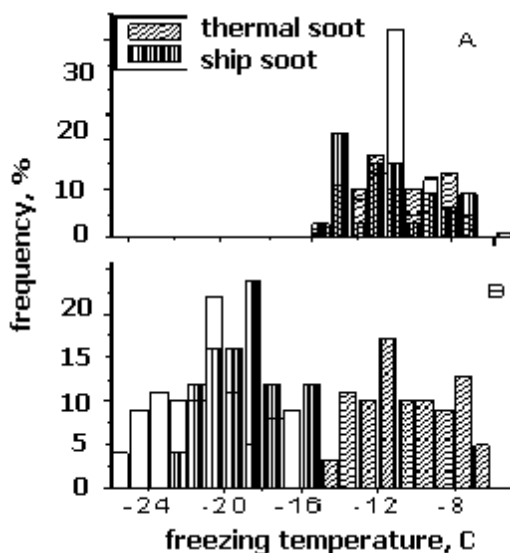


Figure 2. Freezing frequency of A) pure water droplets and droplets with TS and ship soot immersed, of B) pure 10 wt % sulfuric acid droplets and droplets with TS and ship soot immersed.

#### 4 FREEZING OF SULFATE DROPLETS WITH SOOT IMMERSSED

The immersion freezing efficiency of polluted water droplets is determined by the water molecule ability to form hydrogen bonds with the soot surface. In sulfuric acid droplets the soot surface attracts sulfates due to electrostatic or dispersion forces. Mechanism of sulfate interactions is determined by acidic and basic properties of the soot surface. In our study a set of soots with different soot surface acidity is analyzed in respect to heterogeneous freezing efficiency. The maximum of freezing efficiency of  $8.8^{\circ}\text{C}$  is observed for Printex soot with basic surface properties.  $\Delta T_f$  of the neutral soot surface of TS and LB is similar,  $6^{\circ}\text{C}$  and  $6.5^{\circ}\text{C}$ , respectively. Ship soot is characterized by extremely acid surface. For this soot  $\Delta T_f$  is not exceed  $2^{\circ}\text{C}$ . The histograms of the freezing frequency of ship and TS soot polluted sulfuric acid droplets in respect to pure ones are shown in fig. 2B. The comparison of freezing of water and sulfate droplets with TS soot immersed shows the significant difference. Such difference indicates the different mechanism of sulfate/soot and water/soot interactions. Ship soot is found to act as poor ice nuclei in both water and sulfate droplets (fig. 2 A,B). The adsorption of sulfate ions leads to subsequent decrease of the acid concentration in the droplets that relates with a shift of the droplet freezing temperature to more warm value. Therefore, the final significant effect of soot immersion into sulfuric acid droplets is observed.

#### 5 DISCUSSION AND CONCLUSIONS

The link between soot physico-chemical properties and immersion freezing efficiency is established. Soot behaviour in water and extent of soot hydrophilicity determine the water droplet immersion freezing. We suggest that these factors could be considered as key requirements for immersion freezing of cloud droplets together with the wetting parameter and a number of active sites. Deposition of the soot particles on the droplet bottom due to sedimentation instability or on the droplet surface due to a poor wettability limits the efficiency of heterogeneous freezing. Hydrophobic soot with negligible active sites does not promote ice nucleation in the immersion freezing mode. Soluble coverage changes the mechanism of water uptake from water cluster growth on the active sites to the dissolution into soluble surface material. Highly soluble surface compounds of hydroscopic soot, such as sulfates, may be easily dissolved in water leading to loss of the potential freezing efficiency. The most efficient immersion freezing nuclei in the atmospheric water cloud droplets is hydrophilic soot with a significant number of oxygen-containing functional groups but not covered totally by hydrophilic sites and soluble compounds. Quantitatively, we may add the maximum efficiency obtained for hydrophilic soot  $4.2^{\circ}\text{C}$ , to  $4.7^{\circ}\text{C}$  found for a homogeneous sus-

pension of soot and conclude a highest effect about 9°C for the best immersion freezing nuclei which may be hypothesized on the bases of our experimental results.

The efficiency of sulfate droplet immersion freezing is determined by the surface chemistry of soot particles namely by a number of acid and basic groups on the surface. Hydrophobic soot with negligible active sites and hydrophilic soot with a number of oxygen-containing functional groups are proposed to act as the most efficient immersion ice nuclei in the sulfate droplets. Hydrophilic soot with significant number of active sites slightly attracts sulfate ions from solution and can not change significantly the acid concentration. Particles of aviation and ship soot are not efficient ice nuclei both in water and sulfuric acid droplets because of the large amount of WSF dissolving in droplet environment.

## 6 ACKNOWLEDGEMENTS

This research was funded by EU FP6 Project QUANTIFY-TTC 003893.

## REFERENCES

- DeMott, P.J., Rogers, D.C., Kreidenweis, S.M., 1997: The susceptibility of ice formation in upper tropospheric clouds to insoluble aerosol components. *J. Geophys. Res.* 102 (D16), 19575–19584.
- Persiantseva, N.M., Popovicheva, O.B., Shonija, N.K., 2004: Wetting and hydration of insoluble soot particles in the upper troposphere. *J. Environ. Monit.* 6, 939–945.
- Popovicheva, O.B., Persiantseva, N.M., Lukhovitskaya, E.E., Shonija, N.K., Zubareva, N.A., Demirdjian, B., Ferry, D., Suzanne, J., 2004: Aircraft engine soot as contrail nuclei. *Geophys. Res. Lett.* 31, L11104.
- Popovicheva, O.B., Kireeva, E.D., Persiantseva, N.M., Khokhlova, T.D., Shonija, N.K., Tishkova, B., Demirdjian, B., 2008: Effect of soot on immersion freezing of water and possible atmospheric implications. *Atmospheric Research* 90, 326–337.
- Popovicheva, O.B., Kireeva, E. D., Shonija, N. K., Zubareva, N. A., Persiantseva, N. M., Tishkova V., Demirdjian, B. , Moldanová, J., V. Mogilnikov, V. Ship particulate pollutants: characterization in terms of environmental implications. *J. Environ. Monit.* Doi:10.1039/B908180A
- Strom, J. and S. Ohlsson, 1998: In situ measurements of enhanced crystal number densities in cirrus clouds caused by aircraft exhaust. *J. Geophys. Res.* 103, 11355–11361.

# Large Eddy Simulation of Persistent Contrails

A.D. Naiman\*, S.K. Lele, F. Ham, J.T. Wilkerson, M.Z. Jacobson  
*Stanford University, Stanford, CA, USA*

**Keywords:** large eddy simulation, contrails, climate modelling

**ABSTRACT:** A study of three-dimensional contrail evolution has been conducted using a large eddy simulation (LES) model. The LES solves the incompressible Navier-Stokes equations with a Boussinesq approximation for buoyancy forces. Contrail ice particles are modelled using a Lagrangian tracking approach along with a microphysical model of growth due to ice deposition and sublimation. Initial condition flow fields approximate the wake of a commercial jet one second after the aircraft has passed. We present results of simulations to 1200 seconds after emission. We find that higher levels of turbulence and shear promote mixing of the aircraft exhaust with ambient air, resulting in faster growth of contrail ice particles and wider dispersion of the exhaust plume when the ambient air is supersaturated. These results provide sensitivity information that is used to refine a subgrid model of aircraft exhaust plume dynamics for use within a global climate model.

## 1 INTRODUCTION

Aircraft are unique among anthropogenic sources of air pollution in that they consume much of their fuel at a cruise altitude near the tropopause, where exhaust has a long residence time and conditions are conducive to the formation of condensation trails (contrails). The effect of contrails and related aviation-induced cloudiness on climate is highly uncertain. The most recent assessment of the effect of aviation on global radiative forcing lists the level of scientific understanding as “low” for linear contrails and as “very low” for induced cloudiness (Lee et al., 2009). The range of estimates for these effects is large, and if the upper end of the range was realized, it would nearly double the overall forcing of aviation.

This paper presents work that is aimed at reducing the uncertainty in these estimates related to understanding the formation and persistence of contrails. We present results from a large eddy simulation (LES) model of contrails that tracks ice particles using a Lagrangian approach. The model has been used to simulate contrail development from 1 to 1200 seconds after emission by a passing commercial jet aircraft under several atmospheric conditions.

## 2 LES MODEL OVERVIEW

Several researchers have modelled contrail development using an LES approach, including Lewellen and Lewellen (2001), Paoli and Garnier (2005), Huebsch and Lewellen (2006), Shirgaonkar and Lele (2007). Our LES code solves the three-dimensional, incompressible Navier-Stokes equations with a Boussinesq approximation for buoyancy forces on an unstructured grid. The numerical scheme uses a finite volume spatial discretization and an implicit fractional-step method for time advancement, with second order accuracy in both space and time (Mahesh et al., 2004; Ham et al., 2007). Contrail ice particles are modelled using a Lagrangian tracking approach and a microphysical model of growth due to ice deposition and sublimation, similar to Paoli et al., (2004).

The computational domain is stationary with respect to the ground, so the computation represents a temporal simulation in a triply periodic domain. The coordinate axes are positioned such that the  $y$ -axis is vertical (opposite gravity), the  $z$ -axis points in the flight direction, opposite the cruise velocity, and the  $x$ -axis is the cross-stream direction. The coupled fluid equations are listed below, where  $\mathbf{u} = u\mathbf{i} + v\mathbf{j} + w\mathbf{k}$  is the velocity vector,  $\rho$  is the fluid density,  $p$  is the fluid pressure,  $\mathbf{g}$  is the

---

\* Corresponding author: Alexander D. Naiman, Department of Aeronautics and Astronautics, Stanford University, Durand Building Room 267, 496 Lomita Mall, Stanford, CA 94305, USA. Email: anaiman@stanford.edu

gravitational acceleration vector,  $\mu$  is the dynamic viscosity of air,  $\theta$  is the potential temperature,  $\kappa$  is the thermal diffusivity of air, and  $D_v$  is the diffusivity of water vapour in air.

$$\nabla \cdot \mathbf{u} = 0 \quad (1)$$

$$\rho_0 \frac{D\mathbf{u}}{Dt} = -\nabla p + \rho' \mathbf{g} + \mu \nabla^2 \mathbf{u} \quad (2)$$

$$\rho' = \frac{-\rho_0 \theta'}{\theta_0} \quad (3)$$

$$\frac{D\theta'}{Dt} = -\frac{d\theta}{dy} v + \kappa \nabla^2 \theta' + \omega_T \quad (4)$$

$$\frac{DY'}{Dt} = -\frac{dY}{dy} v + D_v \nabla^2 Y' + \omega_Y \quad (5)$$

$$\omega_T = -\omega_Y L \quad (6)$$

In addition to the typical set of incompressible Navier-Stokes equations (Equations 1-2) with a Boussinesq approximation (Equation 3), two scalar diffusion equations are solved for potential temperature and water vapour density. We decompose these scalars into a reference part ( $\theta_0$ ,  $Y_0$ ), an altitude-varying part ( $\theta(y)$ ,  $Y(y)$ ), and a perturbation part ( $\theta'$ ,  $Y'$ ). The altitude-varying part is prescribed to be a constant gradient for both variables. The diffusion equations are solved for the perturbation part of the scalars (Equations 4-5). Equations 4-5 also include source terms ( $\omega_T$ ,  $\omega_Y$ ) resulting from a coupling to the microphysical equations and related according to Equation 6, where  $L$  is the latent heat of sublimation of ice.

Contrail ice particles are modelled using a Lagrangian tracking approach and a microphysical model of growth due to ice deposition and sublimation. Particles are currently tracked as tracers of the background fluid. This approximation is suitable at early phases of contrail development, when particle relaxation time  $\tau_p = 4\rho_p r_p^2 / 18\mu$  is short compared to flow time scales due to small particle sizes (particle radius  $r_p$  1-10  $\mu\text{m}$ ). For the late stages of simulation, when the largest particles grow to 100  $\mu\text{m}$ , the effects of sedimentation and particle drag will be added in the future.

The model of microphysical growth is described in detail in Shirgaonkar and Lele (2007). In summary, each ice particle is treated as a spherical nucleus over which ice has deposited. Each computational particle represents a collection of physical particles. Coagulation and coalescence are neglected and re-nucleation is allowed. Particle radius changes due to deposition or sublimation of water to or from the particle surface. The growth rate of a single ice particle is calculated using a simple diffusion model from Kärcher et al. (1996). Growth rates are calculated for each computational particle and integrated over the time step. The source term,  $\omega_Y$ , is then calculated by integrating the source of water vapour in each Eulerian control volume.

### 3 SIMULATION DESCRIPTION

Each case described here was simulated as follows. First, a background field of periodic, decaying turbulence was generated. This background field was then scaled such that the energy matched the inertial subrange spectra  $E(k) = 1.7\varepsilon^{2/3} k^{-5/3}$  at the peak wavenumber,  $k_p = 4$ , for the given case turbulent dissipation rate,  $\varepsilon$ . The 2-D wake one second downstream of a Boeing 767, calculated by the Boeing Company and provided by Dr. Steven L. Baughcum, was added to the background field. A series of unstructured, periodic grids was used to simulate the development of the contrail, with grid resolution maximized near the contrail structure and decreased out to the domain boundaries. Results on each grid were interpolated to the next. Maximum resolution ranged from 0.37 m during the early stages of the simulation to 2.96 m in the latest stage. Similarly, total domain size ranged from  $400 \times 400 \times 400 \text{ m}^3$  to  $3200 \times 1600 \times 400 \text{ m}^3$  as the simulation progressed. Grid sensitivity studies showed little variation in results due to these transitions from one grid to the next.

For all of the cases considered here, the potential temperature gradient is stable ( $d\theta/dy = 2.5$  K/km) and the water vapour gradient approximates a constant ambient relative humidity with respect to ice (RHi) of 130%. Ambient conditions were consistent with a cruise altitude of 10.5 km in a standard atmosphere. The peak exhaust temperature was 4.4 K, the peak exhaust water vapour density was  $1.14 \times 10^{-4}$  kg/m<sup>3</sup>, and the peak particle number density was 85,000 per cm<sup>3</sup>. A total of  $8 \times 10^6$  computational particles, each representing  $2.73 \times 10^8$  physical particles, were tracked, giving a total of  $5.8 \times 10^{12}$  per m in the flight direction, and each was initialized with a radius of 0.1  $\mu\text{m}$ . Four cases were simulated, varying the intensity of both ambient turbulence and vertical wind shear. The cases are summarized in Table 1.

Table 1. Summary of simulation cases, which vary initial ambient turbulence and vertical wind shear.

Case		Turbulent Dissipation Rate (m <sup>2</sup> /s <sup>3</sup> )	Vertical Shear (s <sup>-1</sup> )
A	Baseline	0.0001	0
B	High turbulence	0.001	0
C	Moderate shear	0.0001	0.005
D	High shear	0.001	0.01

#### 4 LES RESULTS

The following figures show results from the four simulation cases. Figure 1 shows two sets of plots for case A, the baseline case, and for case C, the moderate shear case – the upper plots are flight-direction averaged contours of ice water content, while the lower plots are vertically integrated ice area density. For the lower plots, the domain has been duplicated in the flight direction in order to give an impression of the contrail as it would appear in the sky.

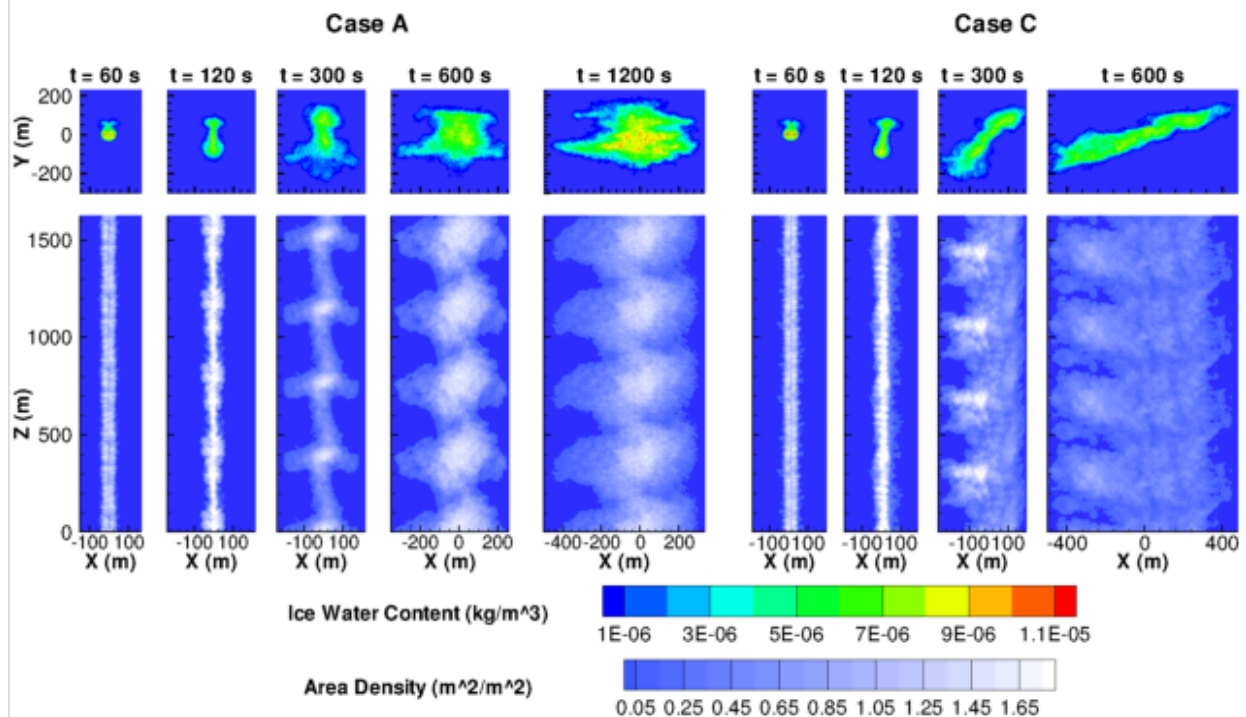


Figure 1. Left plots are for case A, right plots are for case C. Upper plots are flight-direction averaged contours of ice water content. Lower plots are vertically integrated ice area density. Scales and contour levels are identical on all plots.

The overall development of the contrail is as expected. The wake vortices dominate the early flow field and much of the contrail descends with the wake, leaving behind a vertical curtain that detains due to buoyancy. As the Crow instability develops, the vortices are perturbed from their initial linear shapes and eventually link. The pinching off of vortex loops leads to periodic, puffy shapes in the linear contrail. At late times, the decaying ambient turbulence field continues to spread the contrail plume.

Comparison of cases A and C in Figure 1 shows that moderate shear has little effect on vortex behaviour. The vortex wake descends at approximately the same rate, and develops the Crow instability, again forming periodic puffs. As development continues, the contrail is spread horizontally by the vertical shear. An increase in mixing is evident, shown by the reduced separation between the periodic puffs at later times. This mixing is driven by the vertical shear, which reduces the rate at which the ambient turbulent field decays.

Figure 2 shows a comparison of the flight-direction averaged contours of ice water content at the end of the simulation,  $t = 1200$  s, for each of the four cases. The intensity of the ambient turbulence and the vertical shear have a large effect on the contrail cross-sectional shape at late times. More intense ambient turbulence increases cross-sectional area as higher mixing rates spread the contrail (cases A and B). When vertical shear is present, however, it dominates horizontal spreading (cases C and D). These effects are important to understanding the climate impact of contrails, since the horizontal and vertical thicknesses of contrails directly affect the cloud fraction and optical depth attributed to these anthropogenic clouds.

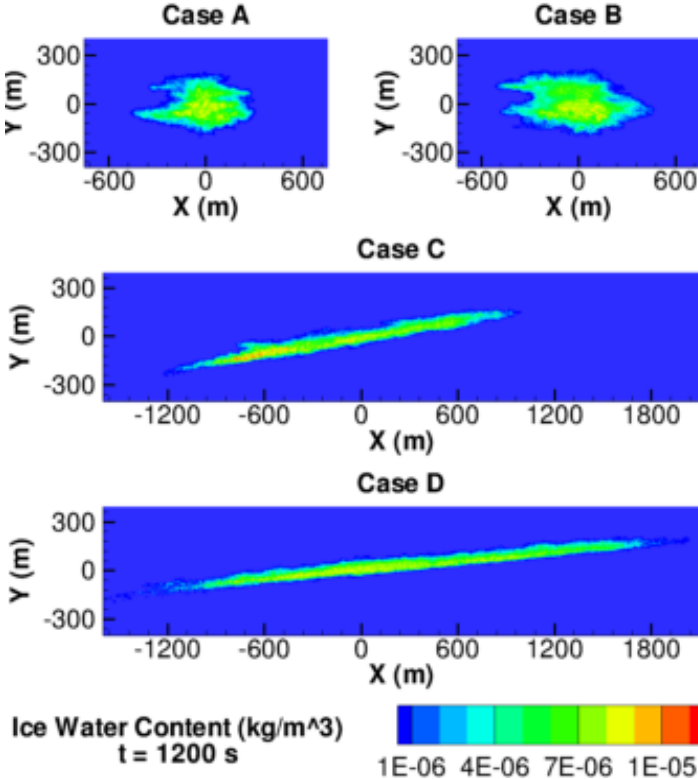


Figure 2. Flight-direction averaged contours of ice water content for each case after 1200 seconds of simulation time.

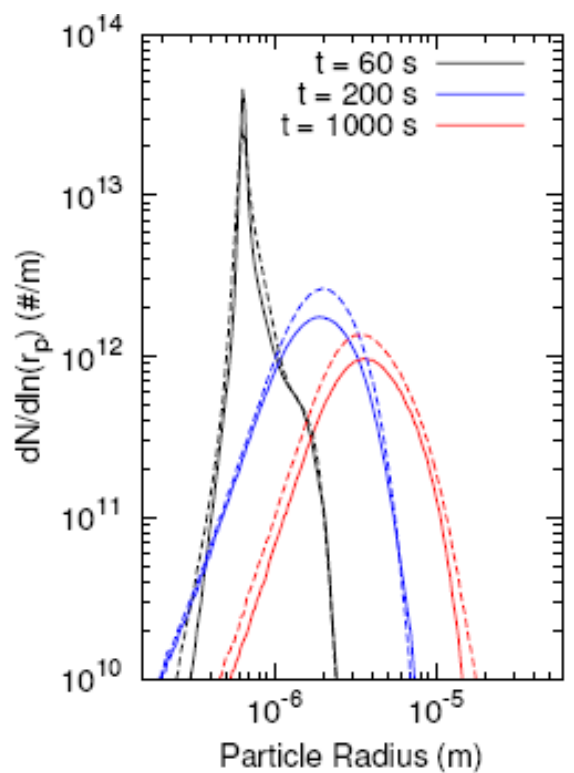


Figure 3. Particle radius distributions at three times during the simulation. Solid lines are for case A, dashed lines are for case D.

Figure 3 shows the size distribution of ice particles integrated over the domain at three times during the simulation for cases A and D. In both cases, as the contrail ages, the spectrum widens and the peak moves to higher radii as ice particles grow. The distribution peak is higher for case D at late times, reflecting the increased ice growth for this case as explained below.

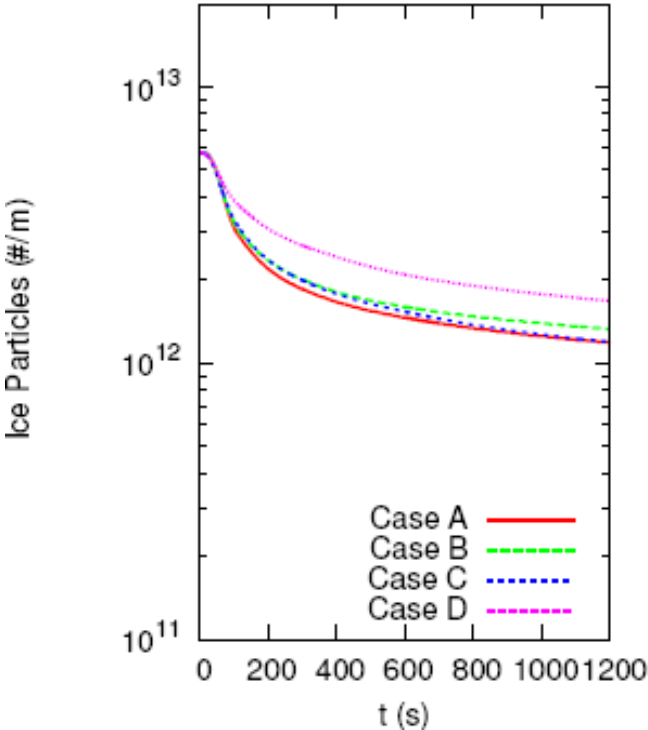


Figure 4. Time history of the domain integrated number of surviving ice particles for each case over 1200 seconds of simulation time.

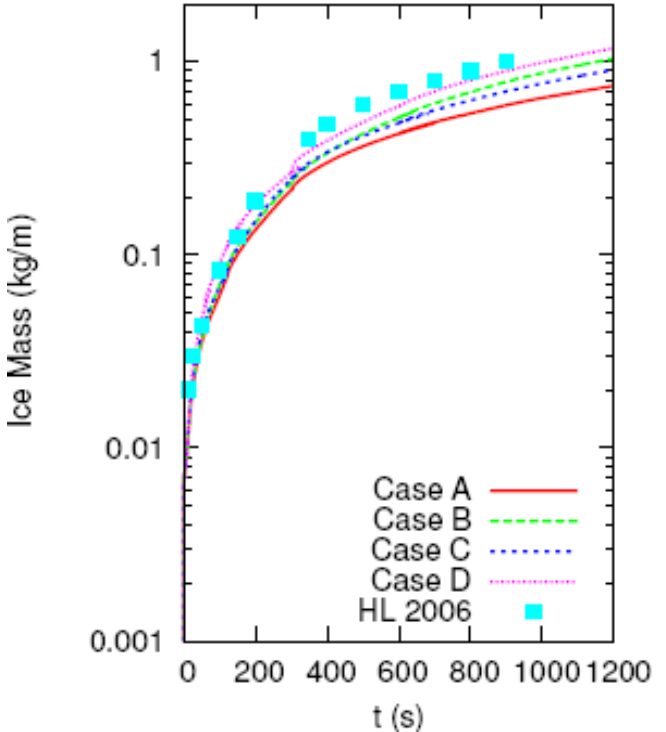


Figure 5. Time history of the domain integrated ice mass for each case over 1200 seconds of simulation time. The HL 2006 data is drawn from Huebsch and Lewellen (2006) for comparison.

Figures 4 and 5 show time history plots of domain-integrated ice statistics. As Huebsch and Lewellen (2006) noted, different turbulent realizations produce variations on the order of 10% in these statistics, so some care should be taken in interpreting the significance of differences between cases.

Figure 4 shows the number of surviving ice particles (that is, ice nuclei from which not all of the ice has sublimated) normalized by the domain length in the flight direction for each case. The number surviving in cases A-C is not significantly different, but case D showed 35% more surviving particles than any of the other cases. Two reasons are likely for this result. First, case D experienced more mixing of ambient air into the contrail than the other cases due to increased forcing of turbulence by its higher shear intensity. Second, the plume experienced more mixing of ambient air into the contrail because of its larger surface area due to its elongated shape. Since the ambient air is highly supersaturated with respect to ice, more mixing into the contrail makes more water vapour available for deposition to particles, resulting in fewer particles completely subliming.

Figure 5 shows the ice water content normalized by the domain length in the flight direction for each case. The total amount of ice deposited during the simulation seems to depend most on the initial level of ambient turbulence, with cases A and C resulting in less ice than cases B and D. The magnitude of ice present at the end of the simulations is similar for each case, and matches well with results presented by Huebsch and Lewellen (2006) under similar conditions. This comparison provides confidence in our results, since the Huebsch and Lewellen simulation used a different LES code that included a binned microphysics model.

## 5 CONCLUSIONS

Our simulations of persistent contrails show the expected results and agree well with previous work. An initial set of four sensitivity cases has shown that ice growth is relatively insensitive to ambient turbulence levels produced by both a decaying isotropic turbulence field and by a linear vertical wind shear. These results have been assimilated into a subgrid contrail model (Naiman et al., 2009) to track contrails within a global climate simulation (Jacobson et al., 2009).

Additional LES cases will vary simulation parameters including aircraft size and engine configuration, and will study the effect of additional microprocesses such as sedimentation. Further study of the sensitivity of contrails to atmospheric and aircraft parameters will allow refinement of the subgrid contrail model for use in future climate studies. Furthermore, these high fidelity simulations will help establish confidence that the low fidelity subgrid contrail model captures the contrail dynamics that are relevant to climate model simulations.

## 6 ACKNOWLEDGEMENTS

This work was supported by the Partnership for AiR Transportation Noise and Emissions Reduction (PARTNER) and the Federal Aviation Administration (FAA) under award number DTFAWA-05-D=0006. Any opinions, findings, and conclusions or recommendations expressed in this material are those of the authors and do not necessarily reflect the views of PARTNER or the FAA. This research is also supported in part by the National Science Foundation through TeraGrid resources provided by LONI and NCSA. The initial flow field was provided by Dr. Steven L. Baughcum of the Boeing Company.

## REFERENCES

- Jacobson, M.Z., J.T. Wilkerson, A.D. Naiman, and S.K. Lele, 2009: Quantifying the effects of aircraft on climate with a model that treats the subgrid evolution of contrails from all flights worldwide. *J. Geophys. Res. – Atmos.*, in review.
- Ham, F., K. Mattsson, G. Iaccarino, and P. Moin, 2007: Towards Time-Stable and Accurate LES on Unstructured Grids. *Lect. Notes Comput. Eng.* 56, 235-250.
- Huebsch, W.W., and D.C. Lewellen, 2006: Application of LES and binned microphysics for sensitivity study on contrail evolution. In: Sausen, R., A. Blum, D.S. Lee, and C. Brüning (eds.): *Proceedings of an International Conference on Transport, Atmosphere, and Climate (TAC)*. Luxembourg, Office for Official Publications of the European Communities, ISBN 92-79-04583-0, 167-172.
- Kärcher, B., Th. Peter, U.M. Biermann, and U. Schumann, 1996: The initial composition of jet condensation trails. *J. Atmos. Sci.* 53, 3066-3083.
- Lee, D.S., et al., 2009: Aviation and global climate change in the 21<sup>st</sup> century. *Atmos. Environ.* 43, 3520-3537.
- Lewellen, D.C., and W.S. Lewellen, 2001: The effects of aircraft wake dynamics on contrail development. *J. Atmos. Sci.* 58, 390-406.
- Mahesh, K., G. Constantinescu, and P. Moin, 2004: A numerical method for large-eddy simulation in complex geometries. *J. Comput. Phys.* 197, 215-240.
- Naiman, A.D., S.K. Lele, J.T. Wilkerson, and M.Z. Jacobson, 2009: A Subgrid Contrail Model for use in Large-Scale Atmospheric Simulations, in preparation.
- Paoli, R., J. Helie, and T. Poinsot, 2004: Contrail formation in aircraft wakes. *J. Fluid Mech.* 502, 361-373.
- Paoli, R., and F. Garnier, 2005: Interaction of exhaust jets and aircraft wake vortices: small-scale dynamics and potential microphysical-chemical transformations. *C.R. Physique* 6, 525-547.
- Shirgaonkar, A.A., and S.K. Lele, 2007: Large eddy simulation of early stage aircraft contrails. Technical Report No. TF-100, Flow Physics and Computational Engineering Group, Department of Mechanical Engineering, Stanford University, 208 pp.

# Uptake of nitric acid in ice crystals in persistent contrails

D. Schäuble\*, C. Voigt, B. Kärcher, P. Stock, H. Schlager

*Deutsches Zentrum für Luft- und Raumfahrt, Institut für Physik der Atmosphäre, Oberpfaffenhofen, Germany*

M. Krämer, C. Schiller, R. Bauer, N. Spelten

*Institut für Stratosphärenforschung, FZ Jülich, Jülich, Germany*

M. de Reus, M. Szakáll, S. Borrmann

*Institut für Physik der Atmosphäre, Johannes-Gutenberg Universität Mainz, Mainz, Germany*

U. Weers, T. Peter

*Institut für Atmosphäre und Klima, ETH Zürich, Zürich, Switzerland*

**Keywords:** Nitric acid, Partitioning, Uptake, Contrails, Cirrus

**ABSTRACT:** This is a short version of Schäuble et al. (2009) published in ACPD. In November 2006 cirrus clouds and almost 40 persistent contrails were probed with in situ instruments over Germany and Northern Europe during the CIRRUS-III campaign. At altitudes between 10 and 11.5 km and temperatures of 211 to 220 K contrails with ages up to 8 hours were detected. These contrails had a larger ice phase fraction of total nitric acid ( $\text{HNO}_3,\text{ice}/\text{HNO}_3,\text{tot} = 6\%$ ) than the ambient cirrus layers (3%). The differences in ice phase fractions between developing contrails and cirrus are likely caused by high plume concentrations of  $\text{HNO}_3$  prior to contrail formation and large ice crystal number densities in contrails. The observed decrease of nitric acid to water molar ratios in ice with increasing mean ice particle diameter suggests that ice-bound  $\text{HNO}_3$  concentrations are controlled by uptake of exhaust  $\text{HNO}_3$  in the freezing plume aerosol in young contrails and subsequent trapping of ambient  $\text{HNO}_3$  in growing ice particles in older (age > 1 h) contrails.

## 1 INTRODUCTION

In the tropopause region the ozone budget is influenced by heterogeneous processes such as the uptake of nitric acid ( $\text{HNO}_3$ ) in cirrus clouds. Results from a global chemistry transport model indicate that  $\text{HNO}_3$  uptake in cirrus ice particles and subsequent particle sedimentation has the potential to remove  $\text{HNO}_3$  irreversibly from this region, leading to a large-scale reduction of gas phase  $\text{HNO}_3$  concentrations (von Kuhlmann and Lawrence, 2006). At typical upper tropospheric  $\text{NO}_x$  levels the irreversible removal of gaseous  $\text{HNO}_3$  reduces the concentrations of the ozone precursor nitrogen oxide ( $\text{NO}_x = \text{NO} + \text{NO}_2$ ) and thus net ozone production rates. Reductions in local ozone concentrations of up to 14 % are found in chemistry box model studies (Meier and Hendricks, 2002).

During several field campaigns from the tropics to the Arctic the interaction of  $\text{HNO}_3$  and cirrus ice crystals was experimentally investigated (e.g. Weinheimer et al., 1998; Popp et al., 2004; Voigt et al., 2006). Voigt et al. (2006) summarized these measurements in terms of average nitric acid to water molar ratios ( $\mu = \text{HNO}_3,\text{ice}/\text{H}_2\text{O}_{\text{ice}}$ ) in cirrus ice particles and ice-bound fractions of total nitric acid ( $\Phi = \text{HNO}_3,\text{ice}/\text{HNO}_3,\text{tot}$ ). Kärcher and Voigt (2006) explained the inverse temperature trend of the  $\mu$  and  $\Phi$  data by means of a model describing nitric acid uptake in growing ice crystals (trapping).

Simulations by Kärcher et al. (1996) indicate the formation of high levels of  $\text{HNO}_3$  in jet aircraft exhaust plumes prior to contrail formation. E.g. Arnold et al. (1992) measured gas phase  $\text{HNO}_3$  in young aircraft plumes. The efficient transfer of gaseous  $\text{HNO}_3$  into plume aerosols and ice particles during contrail formation is demonstrated by Kärcher (1996) by means of microphysical simulations. Gao et al. (2004) measured  $\text{HNO}_3$  in ice particles of a WB-57 aircraft contrail in the subtrop-

---

\* Corresponding author: Dominik Schäuble, Deutsches Zentrum für Luft- und Raumfahrt (DLR) – Institut für Physik der Atmosphäre, Oberpfaffenhofen, D-82234 Wessling, Germany. Email: dominik.schaeuble@dlr.de

ics at 14 – 15 km altitude. They observed  $\text{HNO}_3$  in contrail particles at temperatures below 205 K, presumably in the form of NAT, but did not explicitly report ice phase  $\text{HNO}_3$  concentrations.

An experimental quantification of the  $\text{HNO}_3$  content in contrail ice particles as a function of mean ice particle size, a proxy for the microphysical age of persistent contrails, is lacking. So our observations provide an unprecedented data set on the uptake of  $\text{HNO}_3$  in persistent contrails.

## 2 INSTRUMENTATION

During the CIRRUS-III campaign in November 2006, the Enviscope Learjet performed 5 flights at latitudes between 48°N and 68°N with instruments measuring  $\text{NO}_y$ ,  $\text{H}_2\text{O}$ , small ice crystal size distributions, and condensation nuclei (CN). Total and gas phase  $\text{NO}_y$  were measured based on the chemiluminescence technique with a forward- and a backward-facing inlet, respectively. We calculated the concentration of particulate (in our case essentially ice phase) reactive nitrogen,  $\text{NO}_{y,\text{ice}} = (\text{NO}_{y,\text{forw}} - \text{NO}_{y,\text{back}}) / \text{EF}_{\text{NO}_y}$ , in contrails with a size-dependent relationship for the enhancement factor  $\text{EF}_{\text{NO}_y}(d)$  (Belyaev and Levin, 1974). Nitric acid was directly measured during the flight on 28 November (nylon filter technique). The  $\text{HNO}_3$  concentration on 24 and 29 November was derived from  $\text{NO}_y$  observations and the  $\text{HNO}_3$  to  $\text{NO}_y$  ratio ( $0.45 \pm 0.2$ ) detected on 28 November. This ratio is in good agreement with previous observations in midlatitudes (e.g. Talbot et al., 1999).

In young contrails  $\text{NO}_x$  constitutes the major fraction of  $\text{NO}_y$ . A microphysical plume model study (Meilinger et al., 2005) including detailed heterogeneous aerosol and ice phase chemistry indicates that the chemical conversion into  $\text{HNO}_3$  is small in contrails in terms of the gas phase  $\text{HNO}_3/\text{NO}_y$  ratio ( $\approx 1\%$ ) within the first ten hours after emission due to heterogeneous dehoxification and production of HONO. In such contrails the gas phase  $\text{HNO}_3$  concentration is supposed to be controlled by entrainment of ambient  $\text{HNO}_3$ . Thus, we used the ambient  $\text{HNO}_3$  concentration as an approximation for the concentration inside contrails. In cirrus clouds as well as in contrails,  $\text{HNO}_3$  is assumed to account for 100 % of  $\text{NO}_y$  in ice particles. The uptake of PAN and HONO on ice crystals is probably small compared to  $\text{HNO}_3$  (Bartels-Rausch et al., 2002) and  $\text{N}_2\text{O}_5$  and  $\text{HO}_2\text{NO}_2$  are quickly photolyzed during daytime.

Total water was measured with the forward-facing inlet of the Fast In situ Stratospheric Hygrometer (FISH) (Zöger et al., 1999) and water vapour was detected with a TDL instrument (OJSTER). The Forward Scattering Spectrometer Probe FSSP-100 (Borrmann et al., 2000) measured the number concentration and size distribution of particles with diameters of 2.8 – 29.2  $\mu\text{m}$ .

Contrails were identified from distinct simultaneous short-term increases in the time series of the concentrations of  $\text{NO}_{y,\text{gas}}$ ,  $\text{NO}_{y,\text{tot}}$ , CN ( $> 5$  nm diameter, not discussed here), and ice particles. Lower limits of 0.1 nmol/mol for  $\Delta\text{NO}_{y,\text{gas}}$  and  $100 \text{ cm}^{-3}$  for  $\Delta\text{CN}$  enabled a separation of contrails from cirrus clouds that were not affected by aviation within the last 8 h of their lifetime. Contrails often exhibit significant spatial inhomogeneities in structure and dilution properties. The spatially random sampling of contrails and merging of several individual contrails introduce considerable uncertainty in the exact determination of contrail age from plume dilution data which is difficult to quantify.

## 3 NITRIC ACID PARTITIONING AND ICE WATER CONTENT IN CONTRAILS

European Centre for Medium-Range Weather Forecasts analyses indicate that the top regions of frontal cirrus layers were probed on 24 and 29 November, whereas on 28 November the observations originate from deeper inside cirrus clouds. Figure 1 shows a typical time series of data from the flight on 24 November over Germany.

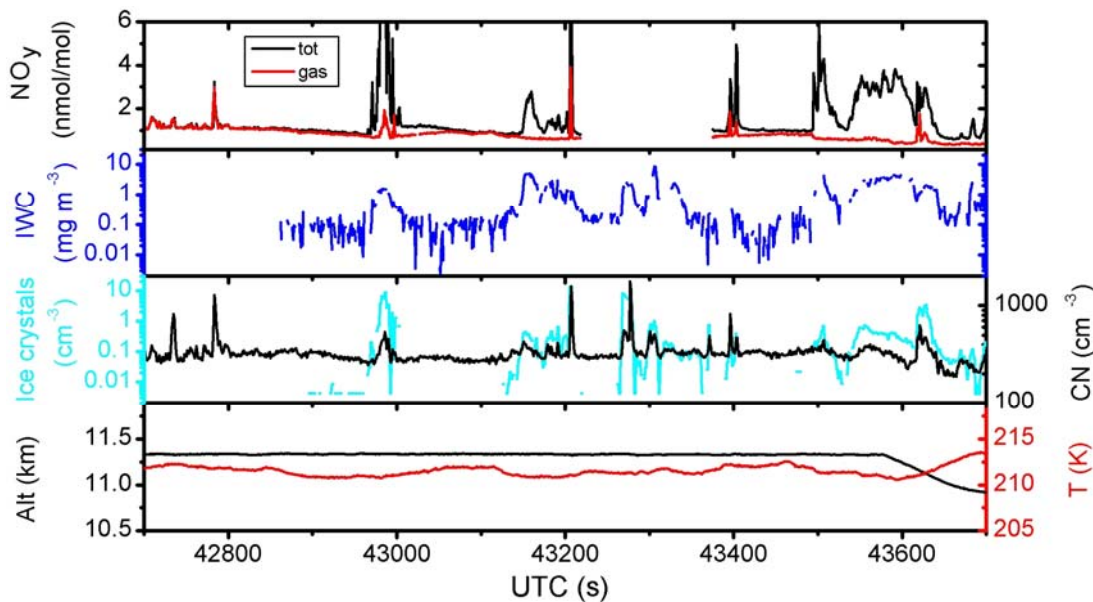


Figure 1. Time series of gas phase and total  $\text{NO}_y$ , ice water content (IWC), number densities of ice particles with approximate diameters between 2.8 and 29.2  $\mu\text{m}$ , CN ( $> 5\text{ nm}$ ) concentration, as well as altitude and temperature for a period of the flight on 24 November 2006. Exhaust plume at 42,780 s, contrails at approximately 42,980 s, 43,200 s, 43,400 s, and 43,620 s, and cirrus clouds around 43,150 s and 43,550 s. Gaps in the  $\text{NO}_y$  measurements are due to calibration procedures.

On average, contrails were found to have larger  $\Phi$  values than the cirrus layers under similar conditions. This is illustrated by means of the probability density function of  $\Phi$  (Fig. 2a). At temperatures between 211 and 220 K, contrail ice particles contained on average 6 % (cirrus 3 %) of the total nitric acid.

Twelve young contrails with  $\Delta\text{NO}_{y,\text{gas}} > 0.75 \text{ nmol/mol}$ , corresponding to ages  $< 1\text{ h}$ , had even larger ice phase nitric acid fractions (9 %). The maximum  $\Phi$  measured in contrails was 22 %. The gas phase equivalent mixing ratio of nitric acid in ice,  $\text{HNO}_{3,\text{ice}}$ , is 14 pmol/mol in contrails compared to 6 pmol/mol in the cirrus layers. The mean  $\text{HNO}_{3,\text{ice}}$  in the young contrails is 21 pmol/mol.

Figure 2b (top panel) shows the temperature dependence of the ice phase molar ratios of nitric acid and water ( $\mu$ ) in contrails (red circles) and in the surrounding cirrus layers (grey circles) that were not recently influenced by aviation. The  $\mu$  values generally increase with decreasing temperature, as the probability of  $\text{HNO}_3$  molecules to escape from the growing ice surfaces after adsorption is reduced at low temperatures leading to more efficient trapping of  $\text{HNO}_3$  (Kärcher and Voigt, 2006).

The curves are results from the trapping model by Kärcher et al. (2009). The dashed and solid model curves were computed for  $\text{HNO}_3$  partial pressures of  $3 \times 10^{-8} \text{ hPa}$  and  $6 \times 10^{-8} \text{ hPa}$ , respectively, roughly capturing the range of measured values occurring in contrails and cirrus (see above). The trapping model bounds the observed mean  $\mu$  values in cirrus (black squares) very well at 211 - 220 K. The model assumes temperature-dependent mean ice particle growth rates (net supersaturations) to estimate steady-state molar ratios. Deviations of individual data points from the mean model curves are likely caused by variable growth/sublimation histories of the observed ice particles. Further, the  $\mu$  of small ice crystals may be strongly influenced by the composition of the freezing aerosol resulting in values exceeding the means (Sect. 4). The mean  $\text{HNO}_3/\text{H}_2\text{O}$  molar ratio in contrails of  $4 \times 10^{-6}$  is found to be approximately twice as large as in the cirrus layers ( $2 \times 10^{-6}$ ).

Figure 2b (bottom panel) illustrates the IWC of contrails and cirrus clouds versus temperature. The difference between the CIRRUS-III IWCs and the climatological means (solid curve) by Schiller et al. (2008) are discussed in Schäuble et al. (2009). The contrails have a slightly larger mean IWC (red squares) than the cirrus clouds,  $1.8 \text{ mg m}^{-3}$  and  $1.3 \text{ mg m}^{-3}$ , respectively. The IWC of young contrails  $2.9 \text{ mg m}^{-3}$  is more than twice the cirrus mean. The  $\text{H}_2\text{O}$  aircraft emissions become unimportant for contrails older than a few minutes, according to plume dilution estimates (Gerz et al., 1998). Differences between contrail and cirrus IWCs are expected to diminish over time as most of the  $\text{H}_2\text{O}$  in contrail ice condenses from the ambient air during ice particle growth.

We additionally report a striking difference between measured contrail and cirrus cloud ice particle number densities in the FSSP-100 size range 2.8 - 29.2  $\mu\text{m}$  in diameter,  $1.5 \text{ cm}^{-3}$  and  $0.21 \text{ cm}^{-3}$ ,

respectively. Figure 3a shows the increase of the ice-bound nitric acid fraction with increasing ice crystal number densities in contrails (means in black). Together this is one explanation for the larger  $\Phi$  in contrails compared to cirrus.

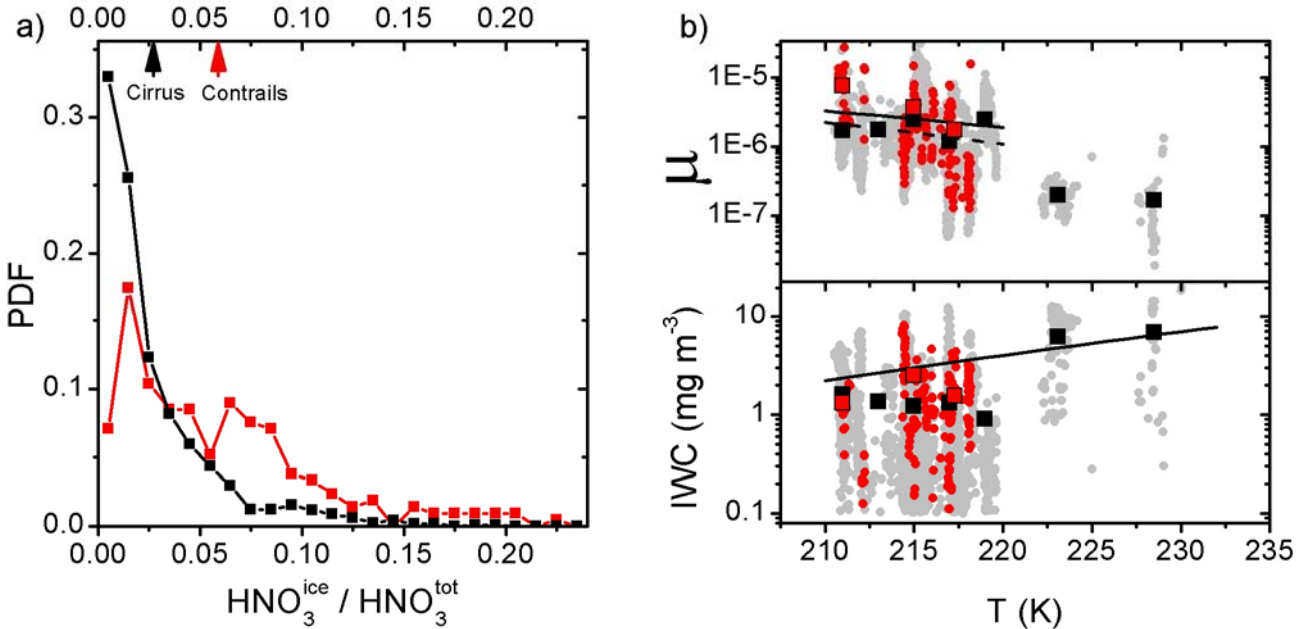


Figure 2. a) Normalized probability density function of the ice phase fraction of total  $\text{HNO}_3$ ,  $\Phi$ , for contrails (red) and cirrus clouds (black). Arrows indicate the means for the temperature range (211 - 220 K) where contrails occurred. b) The temperature dependence of the (top) molar ratio of nitric acid to water in ice particles ( $\mu = \text{HNO}_3, \text{ice} / \text{H}_2\text{O}, \text{ice}$ ) and (bottom) ice water content (IWC) of contrails (red circles) and cirrus clouds (grey circles). Squares are means over 2 K temperature bins. Curves are model results, see text for details. The curve in the bottom panel depicts the mean cirrus IWCs based on a large number of in situ measurements at midlatitudes (Schiller et al., 2008).

#### 4 NITRIC ACID UPTAKE IN DEVELOPING CONTRAILS

Given the limited amount of contrail data, it is unclear whether the systematic differences in ice phase fraction and molar ratios in ice presented in Section 3 are representative. Nevertheless, sorting the molar ratio data as a function of the mean ice particle size enables us to study the  $\text{HNO}_3$  uptake process in contrails in more detail.

Figure 3b shows the molar ratios (grey circles) along with the mean (black squares) and median (grey squares) values of the contrails probed during CIRRUS-III as a function of the mean ice particle diameter. We associate rough estimates of the contrail age with the mean diameter based on the gas phase  $\Delta\text{NO}_y$  data (Schumann et al., 1998), as indicated in the figure. In persistent contrails, the mean size increases due primarily to uptake of  $\text{H}_2\text{O}$  from the gas phase (depositional growth). The measurements show a clear trend of decreasing  $\mu$  with increasing mean size or age. Young contrails with ages 10 – 15 min and mean diameters 7  $\mu\text{m}$  have a mean  $\mu \approx 10^{-5}$ , while older contrails with ages > 1 h and mean diameters > 10 – 15  $\mu\text{m}$  exhibit values closer to the mean  $2 \times 10^{-6}$  of the cirrus data. How are the high molar ratios in young contrails brought about? We argue that a high concentration of  $\text{HNO}_3$  entered the ice particles already during contrail formation, when they are very small (mean diameters 1  $\mu\text{m}$ ), leading to very high molar ratios. Subsequent depositional growth increases the size per ice particle, while trapping in young contrails (mean diameters 1 – 10  $\mu\text{m}$ ) only adds a small contribution to the  $\text{HNO}_3$  content per particle; both effects cause  $\mu$  to decrease in this phase of contrail development. Further growth to larger sizes diminishes the role of the initially high molar ratios and trapping takes over the dominant part in determining  $\mu$ . These processes are illustrated by the model curves as explained in detail in Schäuble et al. (2009).

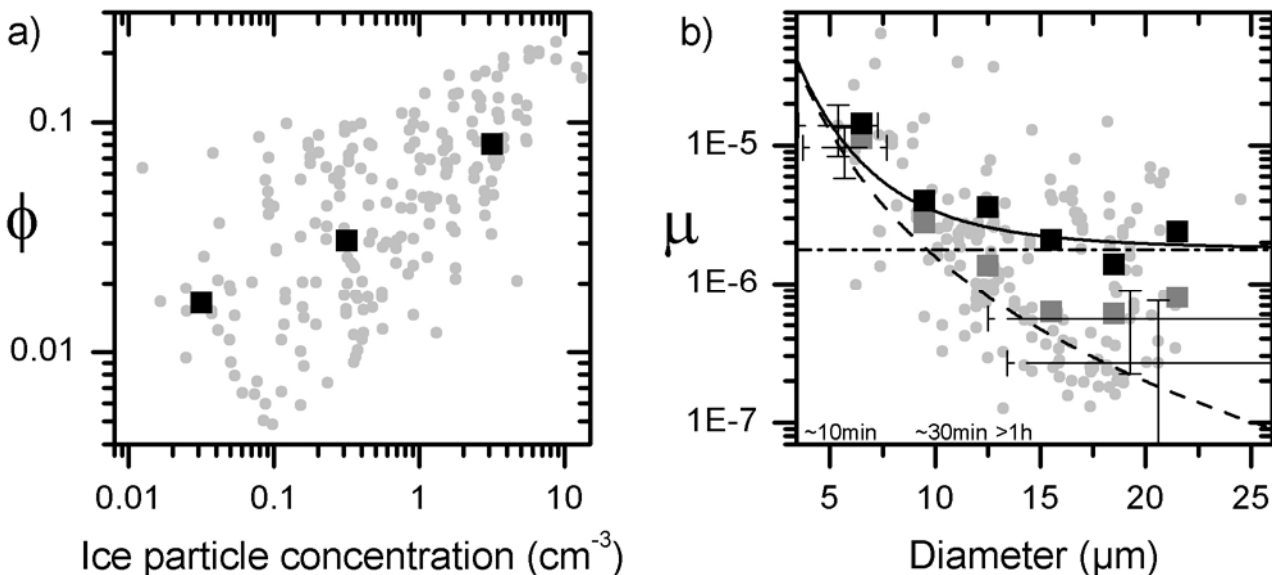


Figure 3. a) Ice-bound nitric acid fraction versus ice crystal number density for mean ice particle diameters between 2.8 and 29.2  $\mu\text{m}$ . b) Molar ratios of nitric acid to water in contrail ice particles  $\mu$  versus mean ice particle diameter. A detailed description is given in Schäuble et al. (2009).

## 5 SUMMARY AND CONCLUSIONS

During the CIRRUS-III field campaign gas phase and ice phase reactive nitrogen, ice water content, and ice crystal size distributions were measured in contrails and cirrus at midlatitudes close to the tropopause. The temperatures and  $\text{HNO}_3$  partial pressures were in the ranges 210 – 230 K and  $3 - 6 \times 10^{-8}$  hPa, respectively. The observed uptake of  $\text{HNO}_3$  in ice particles residing in the top layers of frontal cirrus clouds confirms previous results from airborne field campaigns carried out in polar, midlatitude, and sub-tropical regions (Voigt et al., 2006).

On average the probed contrails contained twice as much ice-bound  $\text{HNO}_3$  as the cirrus clouds within 211 – 220 K, 14 pmol/mol and 6 pmol/mol, respectively. Thus, the mean fraction of total  $\text{HNO}_3$  in ice particles was considerably larger in the contrails (6 %) than in the cirrus layers (3 %). In young contrails (approximate age  $< 1$  h) this fraction was even higher (9 %). The measured molar ratios of  $\text{HNO}_3$  and  $\text{H}_2\text{O}$  in contrail ice particles exceeded  $10^{-5}$  for small particle sizes, or contrail ages. For older contrails, molar ratios approached the mean value of  $2 \times 10^{-6}$  detected in the cirrus layers. Averaged over all detected contrails regardless of age, this caused the mean molar ratios in contrails to be about twice as large as in the cirrus clouds.

Motivated by our study, contrails may be regarded as an atmospheric laboratory to study  $\text{HNO}_3$  uptake during ice particle growth. Our data show that ice phase  $\text{HNO}_3/\text{H}_2\text{O}$  molar ratios decrease during contrail ageing. This dependence was explained by uptake of high levels of  $\text{HNO}_3$  into the freezing aerosol particles during ice formation in contrails and subsequent trapping of relatively low levels of ambient  $\text{HNO}_3$  in growing contrail ice particles. In young contrails with ages  $< 1$  h or mean diameters  $< 10 \mu\text{m}$ , the ice phase  $\text{HNO}_3$  concentrations are therefore largely controlled by the jet engine  $\text{NO}_x$  and  $\text{OH}$  emission indices. More airborne measurements with extended instrumentation are needed to study the dependence of  $\text{HNO}_3$  uptake on  $\text{HNO}_3$  partial pressure and to better quantify ice particle size distributions in developing contrails.

The results of this study help constrain chemical-microphysical models simulating heterogeneous chemistry in persistent contrails in order to constrain the impact of plume processing of  $\text{NO}_x$  emissions on the chemical production or loss of ozone.

## REFERENCES

- Arnold, F., J. Scheid, T. Stilp, H. Schlager, and M.E. Reinhardt, 1992: Measurements of jet aircraft emissions at cruise altitude I: the odd-nitrogen gases  $\text{NO}$ ,  $\text{NO}_2$ ,  $\text{HNO}_2$  and  $\text{HNO}_3$ , *Geophys. Res. Lett.*, 19, 2421 - 2424.

- Bartels-Rausch, T., B. Eichler, P. Zimmermann, H. W. Gäggeler, and M. Ammann, 2002: The adsorption of nitrogen oxides on crystalline ice, *Atmos. Chem. Phys.*, 2, 235 - 247.
- Belyaev, S.P. and L. M. Levin, 1974: Techniques for collection of representative aerosol samples, *J. Aerosol Sci.*, 5, 325 - 338.
- Borrmann, S., B. P. Luo, and M. Mishchenko, 2000: Application of the T-matrix method to the measurement of aspherical (ellipsoidal) particles with forward scattering optical particle counters, *J. Aerosol Sci.*, 31, 789 - 799.
- Gao, R. S., P. J. Popp, D. W. Fahey, T. P. Marcy, R. L. Herman, E. M. Weinstock, D. Baumgardner, T. J. Garrett, K. H. Rosenlof, T. L. Thompson, T. P. Bui, B. A. Ridley, S. C. Wofsy, O. B. Toon, M. A. Tolbert, B. Kärcher, T. Peter, P. K. Hudson, A. J. Weinheimer, and A. J. Heymsfield, 2004: Evidence that nitric acid increases relative humidity in low-temperature cirrus clouds, *Science*, 303, 516 - 520.
- Gerz, T., T. Dürbeck, and P. Konopka, 1998: Transport and effective diffusion of aircraft emissions, *J. Geophys. Res.*, 103, 25905 - 25913.
- Kärcher, B., 1996: Aircraft-generated aerosols and visible contrails, *Geophys. Res. Lett.*, 23, 1933 - 1936.
- Kärcher, B. and C. Voigt, 2006: Formation of nitric acid/water ice particles in cirrus clouds, *Geophys. Res. Lett.*, 33, L08806, doi10.1029/2006GL025927.
- Kärcher, B., M. M. Hirschberg, and P. Fabian, 1996: Small-scale chemical evolution of aircraft exhaust species at cruising altitudes, *J. Geophys. Res.*, 101, 15169 - 15190.
- Kärcher, B., J. P. D. Abbatt, R. A. Cox, P. J. Popp, and C. Voigt, 2009: Trapping of trace gases by growing ice surfaces including surface-saturated adsorption, *J. Geophys. Res.*, 114, D13306, doi:10.1029/2009JD011857.
- Meier, A. and J. Hendricks, 2002: Model studies on the sensitivity of upper tropospheric chemistry to heterogeneous uptake of  $\text{HNO}_3$  on cirrus ice particles, *J. Geophys. Res.*, 107, 4696, doi10.1029/2001JD000735.
- Meilinger, S. K., B. Kärcher, and Th. Peter, 2005: Microphysics and heterogeneous chemistry in aircraft plumes - high sensitivity on local meteorology and atmospheric composition, *Atmos. Chem. Phys.*, 5, 533 - 545, 2005.
- Popp, P.J., R. S. Gao, T. P. Marcy, D. W. Fahey, P. K. Hudson, T. L. Thompson, B. Kärcher, B. A. Ridley, A. J. Weinheimer, D. J. Knapp, D. D. Montzka, D. Baumgardner, T. J. Garrett, E. M. Weinstock, J. B. Smith, D. S. Sayres, J. V. Pittman, S. Dhaniyala, T. P. Bui, and M. J. Mahoney,, 2004: Nitric acid uptake on subtropical cirrus cloud particles, *J. Geophys. Res.*, 109, D06302, doi10.1029/2003JD004255.
- Schäuble, D., C. Voigt, B. Kärcher, P. Stock, H. Schlager, M. Krämer, C. Schiller, R. Bauer, N. Spelten, M. de Reus, M. Szakáll, S. Borrmann, U. Weers, T. Peter, 2009: Airborne measurements of the nitric acid partitioning in persistent contrails, *Atmos. Chem. Phys. Discuss.*, 9, 1 - 22.
- Schiller, C., M. Krämer, A. Afchine, N. Spelten, and N. Sitnikov, 2008: Ice water content of Arctic, midlatitude, and tropical cirrus, *J. Geophys. Res.*, 113, D24208, doi10.1029/2008JD010342.
- Schumann, U., H. Schlager, F. Arnold, R. Baumann, P. Haschberger, and O. Klemm, 1998: Dilution of aircraft exhaust plumes at cruise altitudes, *Atmos. Environ.*, 32, 3097 - 3103.
- Talbot, R.W., J. E. Dibb, E. M. Scheuer, Y. Kondo, M. Koike, H. B. Singh, L. B. Salas, Y. Fukui, J. O. Ballenthin, R. F. Meads, T. M. Miller, D. E. Hunton, A. A. Viggiano, D. R. Blake, N. J. Blake, E. Atlas, F. Flocke, D. J. Jacob, and L. Jaegle, 1999: Reactive nitrogen budget during the NASA SONEX mission, *Geophys. Res. Lett.*, 26, 3057 - 3060.
- Voigt, C., H. Schlager, H. Ziereis, B. Kärcher, B. P. Luo, C. Schiller, M. Krämer, P. J. Popp, H. Irie, and Y. Kondo, 2006: Nitric acid in cirrus clouds, *Geophys. Res. Lett.*, 33, L05803, doi10.1029/2005GL025159.
- von Kuhlmann, R. and M. G. Lawrence, 2006: The impact of ice uptake of nitric acid on atmospheric chemistry, *Atmos. Chem. Phys.*, 6, 225 - 235.
- Weinheimer, A. J., T. L. Campos, J. G. Walega, F. E. Grahek, B. A. Ridley, D. Baumgardner, C. H. Twohy, B. Gandrud, and E. J. Jensen, 1998: Uptake of  $\text{NO}_y$  on wave-cloud ice particles, *Geophys. Res. Lett.*, 25, 1725 - 1728.
- Zöger, M., A. Afchine, N. Eicke, M. T. Gerhards, E. Klein, D. S. McKenna, U. Mörschel, U. Schmidt, V. Tan, F. Tuitjer, T. Woyke, and C. Schiller, 1999: Fast in situ stratospheric hygrometers: A new family of balloon-borne and airborne Lyman- $\alpha$  photofragment fluorescence hygrometers, *J. Geophys. Res.*, 104, 1807 - 1816.

# Peculiarities of airplane vortex wakes and condensation trails interaction and their mathematical modeling

A.N. Zamyatin\*, V.T. Dedesh, R.L. Kagarmanov  
*Gromov Flight Research Institute (GFRI)*

A.I. Zhelannikov  
*N.E.Zhukovski Military-air engineering academy*

*Keywords:* vortex wakes, condensation trails, mathematical modeling

**ABSTRACT:** The unique photos, demonstrating air flow peculiarities in aircraft aerodynamic wake vortex, are presented in the report. On the bases of these materials analysis and also basing on obtained in flight the quantitative data and calculation wake models results, there are presented the patterns of air flow development and structure in aircraft aerodynamic wake. It is shown that scheme of formed aircraft wake vortex structure could be presented as two independent air flow areas. These areas are separated by closed current surface. First – more spacious area corresponds to practically plane spiral flows, consisting of two vortices of opposite direction. The second one is located in the small area of vortices axis and corresponds to spatial flow with circumferential flow velocities, analogous to solid body rotation and with intensive alternating axial flows. Presented in the report are pictures, obtained in real flight conditions with the help of visualization, demonstrating interaction of wake vortex and contrail for aircraft of different types. It is shown that depending on engine location at the aircraft, the contrail could practically do not interact with aerodynamic wake, mainly being captured by external vortex flow and dissipated at relatively small distances from aircraft. Contrail could also being captured by external vortex flow, then got to vortices nuclei and hold by them rather long. Examples of mathematical modeling of a vortex wakes of the airplane, based on MDV utilization are presented in the report, in view of influence of engines jets and conditions of an atmosphere. As an example of wakes calculation for airplanes A - 310, A - 380 and SSJ-100, the qualitative agreement of results of calculations and visualization of streams in wakes is shown. It indicates a possibility of usage and perfection of this method of calculation for the purposes of model creation, account of wake vortices interaction with contrails both in near and far wake, down to their destruction.

## 1 AIRFLOW STRUCTURE IN FIRCRAFT WAKE

Schematic of airplane wake development could be divided into several stages: vortex pair formation, inviscid development, disturbances development, viscous development, destruction. Qualitatively, the flow patterns within one stage are identical for all aircraft and flight conditions. In the first stage the vortex sheet rolling-up after the wing occurred with followed vortex system formation, converting then in the pair of contrary rotating vortices. Airflow structure at this stage depends on circulation distribution along the wing. Local aerodynamics peculiarities could noticeably influence wake formation.

The second stage of wake development is characterized by availability of formed pair of intensive vortices. During this stage, viscosity influence on vortex cinematic characteristics is practically absent, vortex system geometry is changed insignificantly and vortex system descends with small, slow varying speed.

The third stage of wake development features varying geometry of vortices axis while its cinematic characteristics remain the same as in previous stage.

Both geometry and cinematic wake characteristics are varied in the forth stage. Explosive distor-

---

\* Corresponding author: Andrey N. Zamyatin, Gromov Flight Research Institute, Zhukovsky t., Moscow Reg., 140186 Russia. Email: frizamyatin@mail.ru

tions start to develop.

Finally, the fifth stage features qualitative change of vortex structure of wake and its conversion either in closed distorted vortical rings or in attenuating disturbances.

The structure of formed wake vortex of airplane in the second, third and forth stages of development could be divided schematically in two independent flow zones. These zones are separated by closed current surface. First – more spacious zone corresponds to practically flat vortical flow, consisting of two vortices of opposite direction. The second one is located in the small zone near vortices axis and corresponds to spatial flow with circumferential flow velocities, analogous to solid body rotation with intensive axial flows. This scheme of wake vortex air flow is good illustrated by experimental results.

With the help of vortex flow visualization in vertical cross section the dynamics of vortex wake development after freely flying model of A-300 aircraft, launched by catapult is shown in Figure 1.1. The process of spiral-like rolling-up of vortex in wake after aircraft half-wing is absolutely evident. It could be seen in vortex center the not visualized flow zone – vortex nucleus, bounded by closed current surface. The nucleus remains invisible because this closed current surface is impermeable.

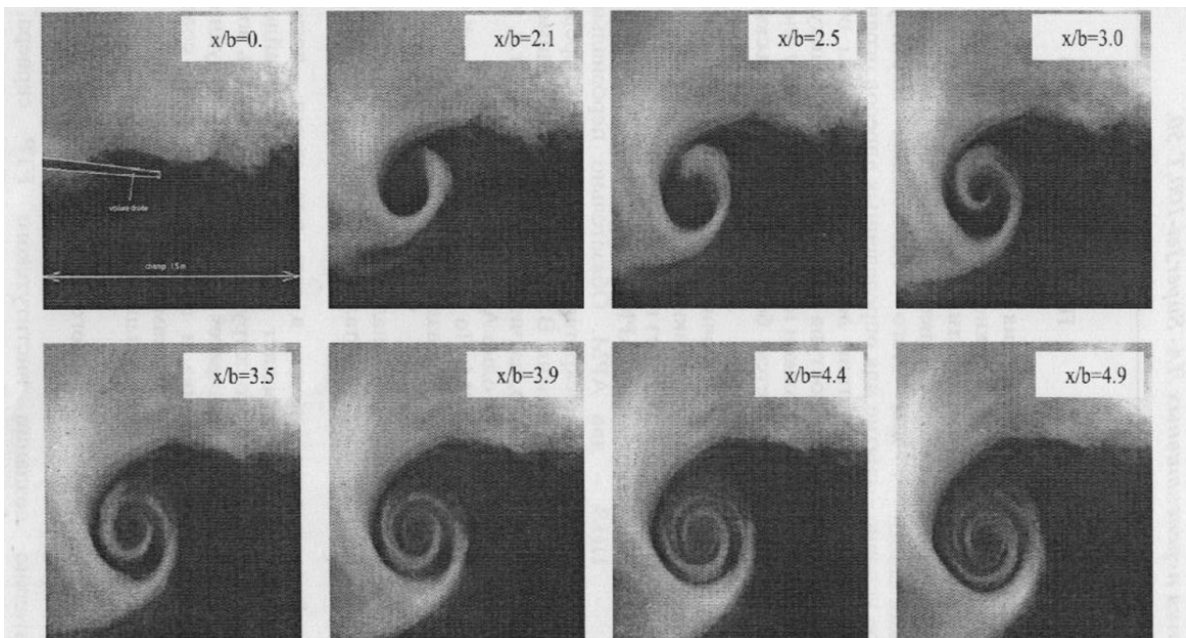


Figure 1.1 The dynamics of vortex wake development after freely flying model of A-300 aircraft  
Analogous flow pattern could be seen in real flights also. Both visualized external flat vortical flow and not visualized vortices nuclei are clearly seen in B-767 airplane wake after flyover through the cloud, see Figure 1.2.



Figure 1.2 Natural visualization of B-767 wake

Having shot a gala firework, the C-17A airplane continuous its flight (Fig. 1.3). Large smoke of pyrotechnics had visualized air flow in wake. Both external vortex motion in wake and free from smoke vortices nuclei could be seen absolutely clear.



Figure 1.3 Artificial visualization of C-17A wake

Visualization of one of vortices in BAe-146 airplane wake had occurred during fly over upward smoke stream, see Figure 1.4. Both zones of air flow in airplane wake again could be observed distinctly.

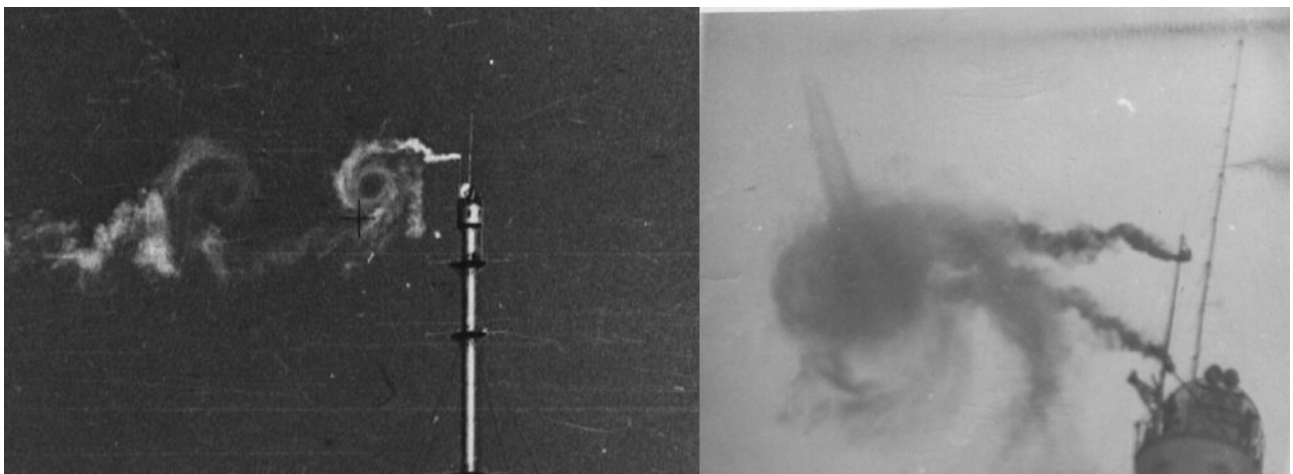


Figure 1.4 Visualization of one of vortices in BAe-146-200A wake at fly over an upward smoke stream

Artificial visualization of external zone of wake vortex was made in special flight research with the help of smoke cartridges, installed in a mast. Pictures of smoke capturing by wake vortices of L-39 and Tu-124 airplanes are shown in Figure 1.5.



**L-39**



**Tu - 124**

Figure 1.5 Smoke visualization of a wake with the help of cartridges, installed in a mast

Again external flow in wake vortex is clearly observed and closed current surface on nucleus boundary prevents air flow visualization in vortices nuclei.

The flow in vortices nuclei could be visualized only in case of visualization source location immediately in vortex nucleus or with the help of wake formation process visualization, that is during visualization of vortex sheet rolling-up.

Sufficiently sharp visualization of flow in vortex nucleus was obtained with the help of artificial visualization, when one of smoke cartridges installed in the mast occurred in the vortex nucleus. Pattern of such flow is shown in Figure 1.6. It is shown the sequence of pictures of aircraft wake smoke visualization, made sideways with small time interval. Red circles depict flow area of visualized vortex pair in case when smoke source has got in nucleus of one of vortices. Both zones of flow were visualized in example presented.



Figure 1.6. Visualization of nuclei zone, when the smoke source has got in nucleus (L-39). Artificial visualization of vortices by smoke generators located at 70...90 % of wing half span provides smoke penetration into vortices nuclei. Nuclei in turn hold smoke inside closed current surface and make the wake visible up to its destruction.

Shown in Figure 1.7 are the smoke visualization of vortices of L-39 and Tu-124 wakes. Smoke generators, mounted in 80% of half wing span under each wing provided vortices nuclei visualization up to wake destruction.

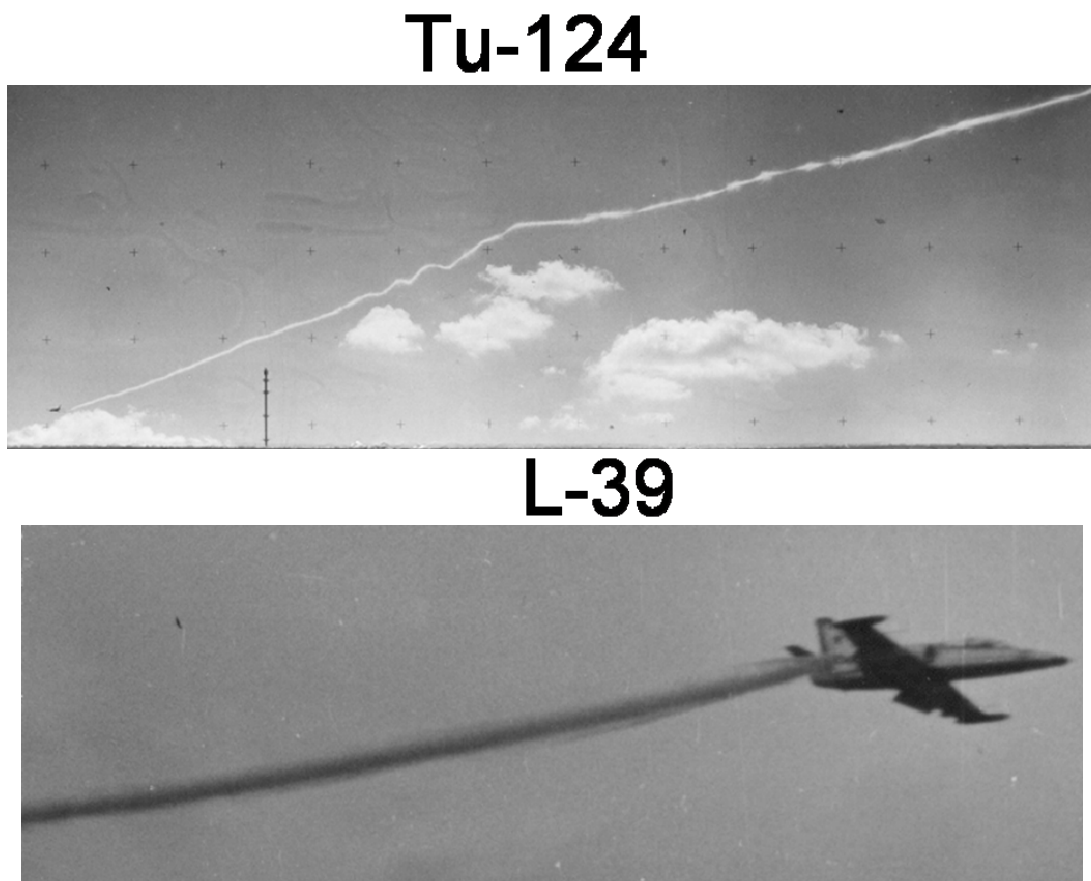


Figure 1.7 Smoke visualization of vortices nuclei

At certain meteorological conditions, the areas of over tenuity become visible. As an example the natural visualizations of zones in nuclei of vortices and also zones over the wings are presented in the next Figure 1.8.



Figure 1.8 Natural visualization of vortex nucleus zone and external zone of flat vortical flow (B-777)

Natural visualization of vortex nucleus zone could expand for long distances up to wake destruction, while conditions for it existence persist. Also observed in the picture is an external flow, visualization of which occurred as a result of local cloudiness capturing.

## 2 AIRCRAFT WAKE VORTICES INTERACTION WITH CONDENSATION TRAILS

Contrails could be captured by vortex flow, penetrate into vortices nuclei and to be hold by it rather long, could be captured by external vortex flow or could practically do not interact with vortex wake depending from aircraft configuration – engines location on the aircraft.

The first situation, when contrails are captured by external vortical flow and penetrate into vortices nuclei and hold by it rather long is illustrated in the Figure 2.1. This picture is observed in case of aircraft with several engines, installed under the wings, like B-747, IL-86 aircraft etc.



Figure 2.1 Capture of contrail by both zones of vortex wake (B-747) (two engines under each wing)

It is evident that contrail capture by vortex flows of aircraft vortex wake occurs at the pictures presented. Engines location is such that vortex wake captures contrail both by its external vortical flow and by vortices nuclei. It seems that conditions for stable existence of contrail disappear and the flow becomes invisible in external zone of vortices at a distance of 5...10 wing spans.

Conditions for stable existence of contrail persist inside closed surface of vortex nucleus and the flow remains to be visible for many kilometers after the airplane (see Figure 2.2).



Figure 2.2 Existence of contrail in nuclei zone at long distance behind IL-86

Shown on the pictures presented is the sufficiently extended visualization of airplane vortex wake, occurred as a result of contrail capture by vortices nuclei what make it possible to trace the development of a wave instability of vortex pair and to observe explosive vortices destructions. But it seems impossible to give an answer to the question of airplane wake vortex destruction influence on captured contrail existence and its conversion in cirrus clouds without additional research.

In case of airplane with engines location one by one under each wing, like B-767, B-777 airplanes, the contrail, as a rule, is captured only by an external zone of vortex flow and exists for a short time. Taking into account the relative geometric position of engines and vortices in B-777 or B-767 airplanes wake the contrail penetration into vortices nuclei is unlikely for airplanes of such configuration. The picture of B-777 aircraft wake in real flight, presented in the Figure 2.3, confirms that, but for more precise results with quantitative data, the additional specially prepared researches are necessary.

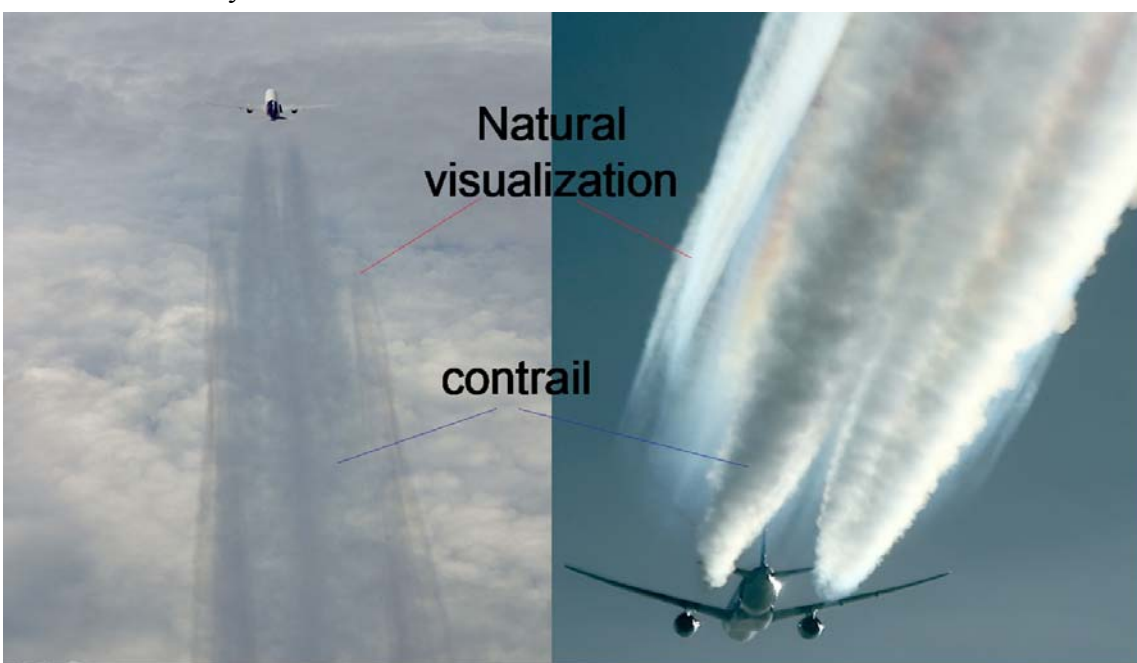


Figure 2.3 Capture of contrail by external vortical zone ( B-777 ) (one engine under each wing)

There is no evident capture of contrail by vortex flow for the airplane with configuration analogous to Tu-154, as it follows from picture on Figure 2.4.



Figure 2.4 Without capture of contrails by vortex wake (Tu-154)  
Used photographic materials are taken from internet and received by authors.

### 3 MATHEMATICAL MODELING OF A WORTEX WAKES OF THE AIRPLANE , BASED ON MDV UTILIZATION IN VIEW OF INFLUENCE OF ENGINES JETS

#### 3.1 Problem statement. Discrete vortex method

Considered here is the unsteady flow of an ideal incompressible fluid past an aircraft flying at the speed  $W_\infty$  (Figure 3.1). The motion of the aircraft and deflection of its control surfaces and high-lift devices are preformed in an arbitrary way. The aircraft's surface is considered impermeable. The flow is potential everywhere outside of the aircraft and vortex wakes generated by flow separation from its surface. The vortex wakes represent thin vortex sheets, i.e., surfaces of discontinuity for the tangential component of the velocity. The lines of flow separation are specified.

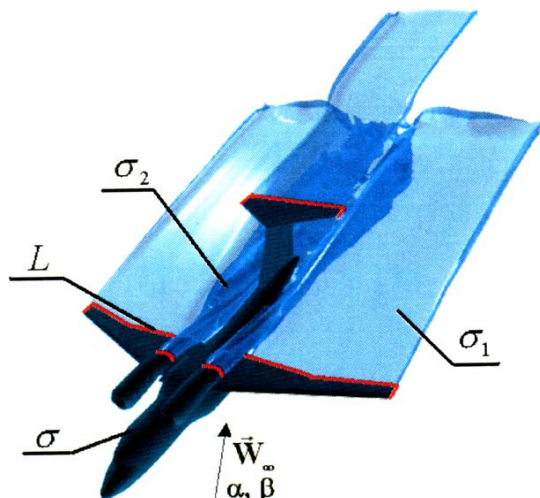


Figure 3.1. Computational model.

Let us denote the lifting and control surfaces of an aircraft together with its engine nacelles by  $\sigma$ , the free vortex sheet shed from the lifting and control surfaces by  $\sigma_1$ , the surface of the exhaust jet by  $\sigma_2$ . The lines of the sheet's shedding are labeled  $L$ .

From a mathematical point of view, the problem at hand is reduced to obtaining in a suitable coordinate system the unsteady fields of the velocities  $\vec{W}(\vec{r}, t)$  and pressures  $p(\vec{r}, t)$ , which must satisfy the following conditions and equations:

- The perturbation velocity potential  $U(\vec{r}, t)$  at every time moment outside of the surfaces  $\sigma$ ,  $\sigma_1$  and  $\sigma_2$  must satisfy the Laplace equation

$$\Delta U = 0, \quad (3.1)$$

- On the surface  $\sigma$ , the flow tangency condition must be met:

$$\frac{\partial U}{\partial n} = -\vec{W}_\infty \cdot \vec{n}; \quad (3.2)$$

- On the vortex wake's surfaces  $\sigma_1$  and  $\sigma_2$ , being the tangential discontinuity surfaces, the condition of zero pressure jump across the wake at every its point and the no-flow condition through the surface must be satisfied:

$$p^+ = p^-, \quad W_n^+ = W_n^- = V_n, \quad (3.3)$$

where  $V_n$  is the normal component of the velocity on the surface  $\sigma_1$ .

- At the separation lines, the Chaplygin-Zhukovsky condition concerning velocity finiteness must be met:

$$\vec{W}_n(\vec{r}, t) \rightarrow 0. \quad (3.4)$$

- At infinity, the disturbances die away:

$$\Delta U \rightarrow 0, \text{ at } \vec{r} \rightarrow \infty; \quad (3.5)$$

- For relation between velocity and pressure, the Bernoulli equation is used:

$$p = p_\infty + \frac{\rho W_\infty^2}{2} - \frac{\rho W^2}{2} - \rho \frac{\partial U}{\partial t}. \quad (3.6)$$

When solving the problem, the potential  $U(\vec{r}, t)$  or  $U(M, t)$  is sought in the form of the double-layer potential

$$U(M_0) = \vec{W}_\infty(t) + \sum_{i=1,2} \frac{1}{4\pi} \int_{\sigma_i} \frac{\partial}{\partial \vec{n}_M} \left( \frac{1}{MM_0} \right) g_i(M, t) d\sigma_M, \quad (3.7)$$

where  $g_i(M, t)$  is the density of the double-layer potential on the surface  $\sigma$ . In this case the fluid velocity at every point not lying on the surfaces  $\sigma$ ,  $\sigma_1$  and  $\sigma_2$  is determined by the formula

$$\vec{W}(M_0, t) = \vec{W}_\infty + \sum_{i=1,2} \frac{1}{4\pi} \int_{\sigma_i} \nabla_{M_0} \left( \frac{\partial}{\partial \vec{n}_M} \left( \frac{1}{r_{MM_0}} \right) \right) g_i(M, t) d\sigma_M. \quad (3.8)$$

Relationship (3.8) is also true on the surfaces  $\sigma$ ,  $\sigma_1$  and  $\sigma_2$  if the integrals involved in it are meant as hypersingular in the sense of Hadamard's finite value. It will be recalled that the double-layer potential undergoes a jump on surfaces where it is defined, but its normal derivative is continuous. Correspondingly, the velocity field has a jump in the tangential velocity component on the surfaces of the schematized aircraft and its wake, whereas the normal component on these surfaces is continuous.

To satisfy conditions (3.3), we seek such a solution where the surfaces  $\sigma_1(t)$  and  $\sigma_2(t)$  consist of points moving together with the fluid, and the density of the double-layer potential,  $g_i(M, t)$ , at

every such point does not depend on time. Suppose that at each instant of time  $\tau \leq t$  a fluid particle leaves the line of wake-shedding,  $M(s)$ , where  $s$  is the arc length, and at the instant  $t$  occupies the position  $M(s, \tau, t)$ , and at each instant  $t$  the totality of the points  $M(s, \tau, t)$  forms the surface of the vortex wakes  $\sigma_1(t)$  and  $\sigma_2(t)$ . In this case the equation of motion for these surfaces takes the form:

$$\frac{\partial \vec{r}(s, \tau, t)}{\partial t} = \vec{W}(M(s, \tau, t), t), \tau \leq t, s : M(s) \in L \quad (3.9)$$

with the initial conditions

$$\vec{r}(s, \tau, t) \Big|_{t=\tau} = \vec{r}_{M(s)}, \quad (3.10)$$

where  $\vec{r}(s, \tau, t)$  and  $\vec{r}_{M(s)}$  are the position vectors of the points  $M(s, \tau, t)$  and  $M(s)$ , respectively, whereas for the function  $g_2(M, t)$  the following relation is true:

$$g_2(M(s, \tau, t), t) \equiv g_2(s, \tau), \tau \leq t, s : M(s) \in L \quad (3.11)$$

Condition (3.2) is equivalent to the equation

$$\frac{1}{4\pi} \sum_{i=1}^2 \int_{\sigma_i} \frac{\partial}{\partial \vec{n}_{M_0}} \frac{\partial}{\partial \vec{n}_M} \left( \frac{1}{r_{MM_0}} \right) g_i(M, t) d\sigma_{i,M} = f(M_0), M_0 \in \sigma_1, \quad (3.12)$$

where  $f(M_0) = -\vec{W}_\infty \cdot \vec{n}(M_0)$ .

Finally, the interrelation between the functions  $g_1(M, t)$  and  $g_2(s, t)$  is described by the following formula, resulting from the integrability condition for the velocity field:

$$g_2(s, t) = g_1(M(s), t), s : M(s) \in L. \quad (3.13)$$

Thus, the problem of unsteady separated flow of an ideal fluid past an aircraft is reduced to the solution of the closed system of equations (3.9)-(3.13) for the functions  $\vec{r}(s, \tau, t)$ ,  $g_1(M, t)$ ,  $g_2(s, \tau)$ . With that, if these functions are the solution of the indicated equations, the potential  $U(M, t)$  defined by formula (3.7), the corresponding velocity field  $\vec{W}(M, t)$  defined by expression (3.8), and the pressure  $p(M, t)$  determined by integral (3.6) satisfy conditions (3.1)-(3.6).

The aircraft's geometry was represented with a combination of thin plates and solid elements. The wing and other lifting surfaces are presented schematically as their surfaces, whereas the fuselage and engine nacelles are modeled with solid elements. The plates and solid elements, in turn, are modeled with a double layer of continuously distributed doublet singularity approximated with the network of discrete closed vortex frames. In this case, rectangular vortex frames (cells) are used. Located along the contour of each cell are vortex filaments, whose intensities are unknown. These vortex filaments induce velocities in accordance with the Biot-Savart law. The resulting velocity field is sought in the form of the sum of the velocities induced by all vortex frames modeling the body's surface and its wake and the velocity of the oncoming flow:

$$\vec{W}(\vec{r}, t_k) = \sum_{i=1}^N \Gamma_i(t_k) \vec{W}_i(\vec{r}) + \sum_{m,l} \Gamma_{ml}^1 \vec{W}_{mlk}(\vec{r}) + \vec{W}_\infty, \quad (3.14)$$

$$\vec{W}_i(\vec{r}) = \frac{1}{4\pi} \oint_{\vec{r} \in \partial\sigma_i} \frac{[\vec{r} - \vec{r}_0] \times \vec{dl}}{[\vec{r} - \vec{r}_0]^3}.$$

Thereafter the problem is reduced to determining the intensities of the vortex frames representing the body  $\Gamma_i$  and vortex wake  $\Gamma_{ml}$ , along with the coordinates of corner points of the vortex frames,  $\vec{r}_{m,l}$ . For determining intensities  $\Gamma_i$  for each vortex frame, a control point (collocation point) is established in a special way, for which the flow tangency condition is written. As a result, one obtains the following system of algebraic equations for  $\Gamma_i$ :

$$\sum_{i=1}^N \Gamma_i(t_k) \omega_{ij} = f_j^k, \quad j = 1 \dots N, \quad (3.15)$$

$$\omega_{ij} = \vec{W}_i(\vec{r}_j) \vec{n}_j, \quad f_j^k = \left[ - \sum_{m,l} \Gamma_{ml}^1 \vec{W}_{mlk}(\vec{r}_j) - \vec{W}_\infty \right] \vec{n}_j. \quad (3.16)$$

When simulating the vortex wake, it is assumed that the vortex frames moves together with fluid particles, and as this takes place, their intensities  $\Gamma_{m,l}$  remain constant:

$$\vec{r}_{ml}(t_k) = \vec{r}_{ml}(t_{k-1}) + \vec{W}(\vec{r}_{ml}(t_{k-1}), t_{k-1}) \Delta t, \quad l < k \quad (3.17)$$

At each instant of time, a new vortex cell forms with its two corner points lying on the separation line:

$$\vec{r}_{kl}(t_k) = \vec{r}_l^L, \quad (3.18)$$

and the intensity of the vortex filament of the newly shed frame is determined through the intensities of the vortex filaments lying on the body's surface and having with it a common side:

$$\Gamma_{ml} = \Gamma_{i^+}(t_m) - \Gamma_{i^-}(t_m). \quad (3.19)$$

In formulas 3.14-3.19,  $l$  is the number of the segment of the separation line left by the frame  $b_{m,l}$ ,  $m$  is the point in time at which the frame leaves the line.

Thus, the solution of the problem is obtained by time stepping until the specified end of computation. At each step, the loads are computed through the Cauchy-Lagrange integral.

The problem in hand is solved by the DVM according to which a flow-immersed body and its wake are replaced with systems of bounded and free vortices (Figure 3.2). In this case, the closed rectangular vortex frames (cells) are used as hydrodynamic singularities (Figure 3.3).

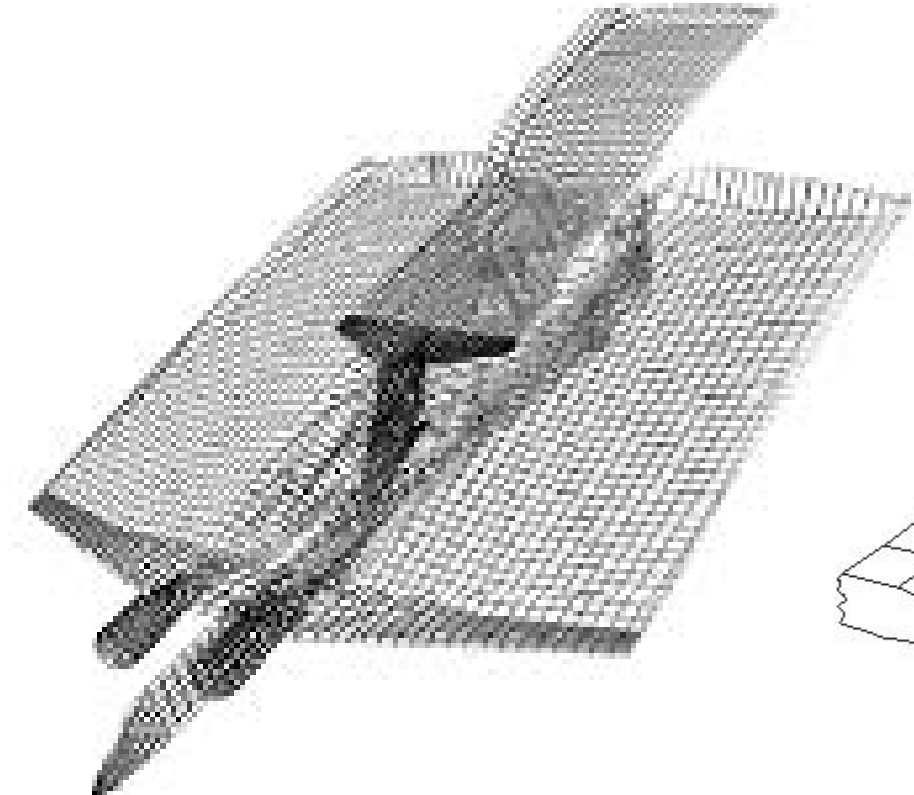


Figure 3.2. System of vortex frames.

Positioned along the contour of each cell  $i$  is a vortex filament whose intensity is unknown. The vortex filaments induce velocities according to the Biot-Savart law. The combined velocity field is

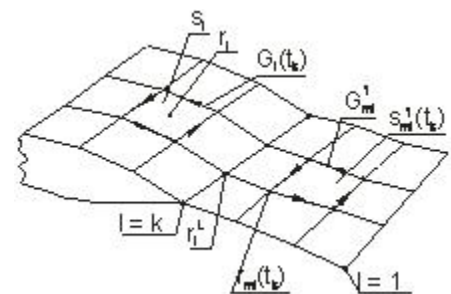


Figure 3.3. Closed vortex frames.

sought as the sum of the velocities induced by all vortex frames modeling the body's surface and its wake and the velocity of the oncoming flow:

$$\vec{W}(\vec{r}, t_k) = \sum_{i=1}^N \Gamma_i(t_k) \vec{W}_i(\vec{r}) + \sum_{m,l} \Gamma_{ml}^1 \vec{W}_{mlk}(\vec{r}) + \vec{W}_\infty, \quad (3.20)$$

$$\vec{W}_i(\vec{r}) = \frac{1}{4\pi} \oint_{\vec{r} \in \partial\sigma_i} \frac{[\vec{r} - \vec{r}_0] \times d\vec{l}}{[\vec{r} - \vec{r}_0]^3}.$$

Thereafter the problem is reduced to determination of the intensities of the vortex frames representing the body  $\Gamma_i$  and vortex wake  $\Gamma_{ml}$  along with the coordinates of the corner points of the vortex frames  $\vec{r}_{ml}$ . For determination of intensities  $\Gamma_i$  for each vortex frame, a control point (collocation point) is specified in a special way, for which the flow tangency condition is written. As a result, one obtains the following system of algebraic equations in  $\Gamma_i$ :

$$\sum_{i=1}^N \Gamma_i(t_k) \omega_{ij} = f_j^k, \quad j = 1, N \quad (3.21)$$

$$\omega_{ij} = \vec{W}_i(\vec{r}_j) \vec{n}_j, \quad f_j^k = \left[ - \sum_{m,l} \Gamma_{ml}^1 \vec{W}_{mlk}(\vec{r}_j) - \vec{W}_\infty \right] \vec{n}_j. \quad (3.22)$$

When modeling the vortex wake, it is assumed that the vortex frames moves together with fluid particles and as this takes place their intensities  $\Gamma_{ml}$  remain constant:

$$\vec{r}_{ml}(t_k) = \vec{r}_{ml}(t_{k-1}) + \vec{W}(\vec{r}_{ml}(t_{k-1}), t_{k-1}) \Delta t, \quad l < k. \quad (3.23)$$

At each instant of time, a new vortex cell is formed with its two corner points lying on the separation line (3.24):

$$\vec{r}_{kl}(t_k) = \vec{r}_l^L, \quad (3.24)$$

and the intensity of the vortex filament on the newly shed frame is determined through the intensities of the vortex filaments lying on the body's surface and having with it a common side:

$$\Gamma_{ml} = \Gamma_{i^+}(t_m) - \Gamma_{i^-}(t_m). \quad (3.25)$$

In formulas (3.20)-(3.25),  $l$  is the number of the segment of the separation line left by the frame  $b_{ml}$ ,  $m$  is the point in time at which the frame leaves the line.

Thus, the solution of the problem is obtained by time stepping until the specified final time step is made. At each step, the loads are computed through the Cauchy-Lagrange integral. These loads are averaged over time when needed.

### 3.2 Aircraft geometry representation

The schematic representation of an aircraft's geometry is an important part of modeling the flow around the aircraft and its vortex wake. The present report generalizes the approaches of many researchers employing the DVM. Among the types of aircraft representation developed up to now, the following three are the most popular and successful: plate-element, solid-element and hybrid representations.

The plate-element representation idealizes an aircraft as an array of thin plates. Each solid element of the aircraft (fuselage, engine nacelles) is represented by two mutually perpendicular plates ("cruciform scheme"). This simplest representation gives good results in many cases, including the prediction of the behavior of an aircraft encountering the wake of another aircraft.

The solid-element representation considers all components of an aircraft (fuselage, engine nacelles, wing, stabilizer, fin) as a combination of solid elements. This is the most complicated representation, but it practically always gives good results, especially in predicting the motion of aircraft.

Presently, the most popular aircraft representation is the hybrid one. In this case the fuselage and engine nacelles are considered as solid elements, whereas the horizontal tail, fin and other lifting and control surfaces are treated as thin plates. Experience has shown that the best results are obtainable if the element representing the wing is bent according to its mean-camber surface.

### 3.3 The characteristics of the near vortex wake behind some aircraft

For predicting of flow around aircraft and obtaining the characteristics of their vortex wakes, nonlinear unsteady theory, based on the DVM was employed. Some works contain the results of computation of aircraft near wakes with the help of linear and nonlinear steady theories. The computational results for the near vortex wake were obtained using a nonlinear unsteady theory, the most general and universal.

Shown in Figure 3.4 is the near vortex wave in view of influence of engines jets generated by the A-310 aircraft at  $\alpha = 7^\circ$ . Thin plates were used to represent the lifting and control surfaces of the aircraft, solid elements modeled the fuselage and engine nacelles. The high-lift devices are deflected for landing. From calculation results it is visible, that in near vortex wave engines jets generated by the A-310 practically do not interact with vortex wake.

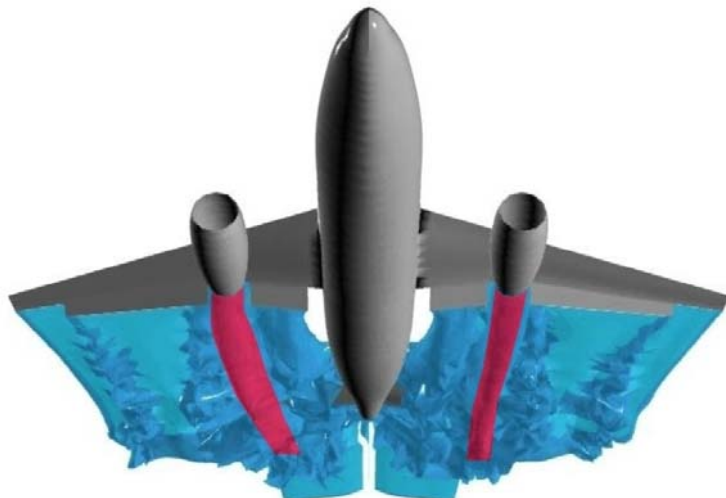


Figure 3.4. Vortex wave generated by the A-310 aircraft at  $\alpha = 7^\circ$ .

The near vortex wake of the A-380 aircraft at  $\alpha = 7^\circ$  in view of influence of engines jets can be seen in Fig. 3.5. Thin plate representation is used for its lifting and control surfaces, the fuselage and engine nacelles are modeled with solid elements. The wing's high-lift devices are in takeoff configuration. It is visible from calculation results, that in near vortex wave engines jets generated by the A-380 starts to be captured by external vortical zone of A-380 aircraft vortex wake.

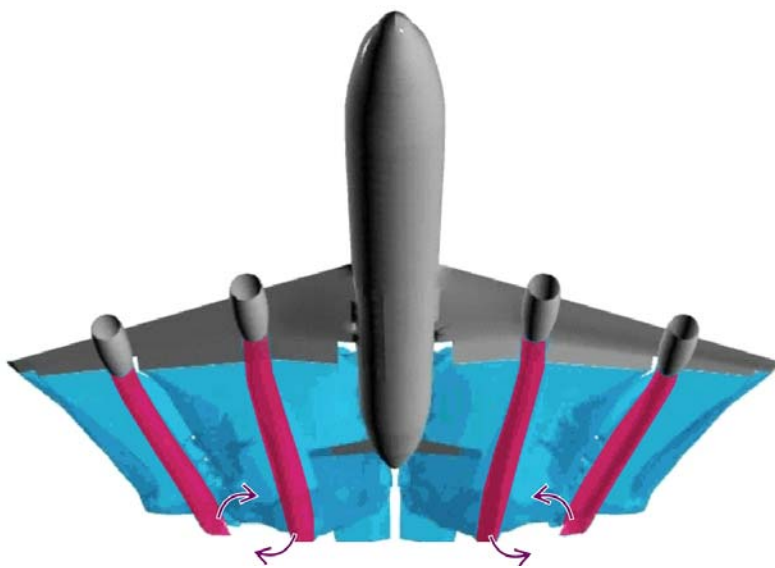


Figure 3.5. Vortex wake of the A-380 aircraft at  $\alpha = 7^\circ$

Figure 3.6 presents the near vortex wake behind the SSJ-100 aircraft at  $\alpha = 20^\circ$  in view of influence of engines jets; lifting and control surfaces are modeled with thin plates, and engine nacelles - with solid elements. In this case capture of the engines jets by near vortex wake also takes place.

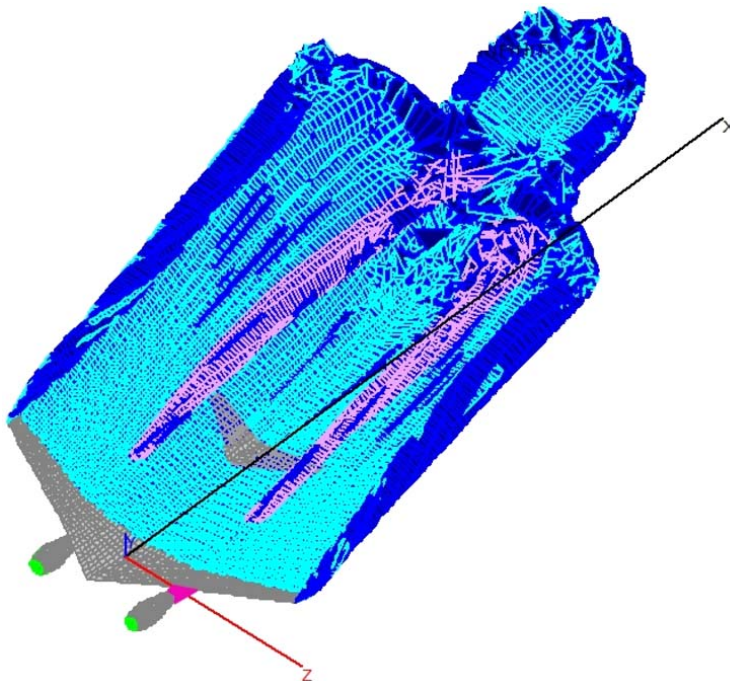


Figure 3.6. Near vortex wake behind the SSJ-100 aircraft at  $\alpha = 20^\circ$

#### 4 CONCLUSIONS

- The analysis of different aircraft wake flow visualization patterns testifies that engines contrails and vortex wake could interact with each other depending on aircraft configuration. This process is essential and it should be taken into account during evaluation of contrail characteristics.
- There is a possibility to model the processes of interaction of vortex wakes with condensation trails by numerical methods, for example by MDV.
- Researches of far interaction of wake and contrails including mathematical modeling will help to study the processes of contrails existence and destruction.

#### REFERENCES

- Aubakirov, T.O., Belotserkovsky, S.M., Zhelannikov, A.I., Nisht, M.I., 1997: *Nonlinear wing theory and its applications*, Almaty, Gylym, 448 pp
- Belotserkovsky, S.M., Dvorak, A.V., Zhelannikov, A.I., Kotovsky, V.N., 1987: *Computer-based simulation of turbulent jets and wakes*. In: *Problems of turbulent flows*, Nauka, Moscow
- Belotserkovsky, S.M., Kotovsky, V.N., Nisht, M.I., Fedorov, R.M., 1988: *Mathematical simulation of separated flows about bodies*, Nauka, Moscow, 232 pp
- Vyshinsky, V.V., Sudakov, G.G., 2006: *Vortex wake of an aircraft in a turbulent atmosphere*, Proc TsAGI # 2667, 155 pp
- Zhelannikov, A.I., 2007: A simplified methodology for computing the far vortex wake behind trunk-route aircraft, Scientific Bulletin of Moscow State Technical University of Civil Aviation, Aeromechanics and Strength # 111, 16 – 21
- Zamyatin, A.N., Soudakov, G.G., 2002: *Colloquium 433, Dynamics of Trailing Vortices*, Theoretical and experimental investigations of external turbulence effect on aircraft vortex wake, Euromech RWTH Aachen, Book of Abstracts, Aachen, Germany
- Babkin, V.I., Belotserkovsky, A.S., Turchak, L.I., Zamyatin, A.N., 2008: *Wake vortex flight safety systems for aircrafts*, Nauka, Moscow, Russia, 373 pp
- Zamyatin A.N., 1991:*Proceedings of the aircraft wake vortices conference*, Real research of different class airplane vortex wakes, U.S. Department of transportation FAA ,Washington, DC, USA